Title
Optimizing district energy systems by integrating Borehole Thermal Energy Storage Using a Mixed-Integer Linear Programming g-function framework with a Multi-Timescale Rolling Horizon method

Journal
Energy, 354

ISSN
0360-5442

Authors
Yang, Jiahui
Soga, Kenichi
Sulzer, Matthias
et al.

Publication Date
2026-07-01

DOI
10.1016/j.energy.2026.141111

Energy 354 (2026) 141111

Contents lists available at ScienceDirect

Energy

journal homepage: www.elsevier.com/locate/energy

Optimizing district energy systems by integrating Borehole Thermal Energy Storage Using a Mixed-Integer Linear Programming g-function framework with a Multi-Timescale Rolling Horizon method

Jiahui Yang [a,*], Kenichi Soga [a], Matthias Sulzer [b], Kecheng Chen [a]

[a] Department of Civil and Environmental Engineering, University of California, Berkeley, Davis Hall, Berkeley, 94720, CA, USA
[b] Urban Energy Systems Laboratory, Empa-Swiss Federal Laboratories for Materials Science and Technology, Überlandstrasse 129, Dübendorf, 8600, Zurich, Switzerland

ARTICLE INFO

Keywords:
Mixed integer linear programming (MILP)
Distributed energy system (DES) optimization
Borehole thermal energy storage (BTES)
The g-function method
Rolling horizon with multi-timescale (RH-MTS) method
Modelica validation
UC berkeley energy system
BTES long-term performance

ABSTRACT

Shallow geothermal has gained increasing attention in recent years; however, a reliable framework for its accurate incorporation into large-scale energy system optimization remains lacking. This study proposes a Mixed-Integer Linear Programming (MILP) framework combined with the g-function approach to integrate Borehole Thermal Energy Storage (BTES) technology into energy system optimization. Validation against a Modelica-based reservoir network simulation demonstrates that the proposed framework effectively captures the ground thermal response under varying energy loads and accurately estimates the borefield energy supply. To enhance scalability, a Rolling Horizon with Multi-Timescale (RH-MTS) method is further introduced, reducing computational time by 73 % for the 1-year optimization model with only minor loss of optimality. The framework is demonstrated through the case study of the UC Berkeley campus. Results indicate that BTES is a cost-effective and low-carbon solution: two borefields comprising 382 boreholes can meet 8.0 % and 6.6 % of the total campus heating and cooling demand, respectively, at an average energy rate of 0.70–0.77 USD/kWh and carbon intensity of 0.54 kg-CO_2/kWh. Short-term analysis reveals a 35%–65% decline in BTES energy flow after 3–6 months of continuous heating/cooling operation, while long-term simulation shows that annual energy production of BTES can vary by up to 12.0 % after four years before stabilizing. Overall, this study develops a novel optimization framework that couples physics-based g-function method with MILP optimization framework, thereby advancing methodological development for shallow-geothermal integration and providing actionable guidance for BTES deployment in district-energy systems.

1. Introduction

The global transition toward low-carbon energy systems has intensified the demand for renewable alternatives to fossil fuels [1,2]. Space heating and cooling constitute a large share of fossil energy consumption – around 18.3% in the United States [3] and over 50% in Europe [4] – yet are predominantly fossil-fuel based, making decarbonization of this energy sector a cornerstone of climate policy. In this context, shallow geothermal energy has emerged as a promising solution due to its high energy efficiency and low greenhouse gas emissions [5].

Shallow geothermal energy systems, particularly Borehole Thermal Energy Storage (BTES), use the subsurface as a seasonal reservoir to decouple supply from demand, reduce peak loads, and enhance the flexibility of District Energy Systems (DES). Compared with other seasonal storage options, BTES has demonstrated superior economic performance [6], proven effective in fifth-generation district heating and cooling networks [7], and maintained high performance over long operating periods [8]. Successful applications have been reported across Europe and North America [6,9–12]. Recent research has increasingly focused on the co-simulation frameworks coupling subsurface models with building or DES simulators, such as TRNSYS-COMSOL, MATLAB-COMSOL, FEFLOW-MATLAB, and Modelica-TOUGH [13–17]. While these high-fidelity approaches capture subsurface physics accurately, they are primarily developed for simulating small-scale DES and are computationally prohibitive for large-scale, long-horizon optimization. This reveals a critical gap in developing tractable yet physically representative methods for modeling subsurface thermal dynamics within large-scale optimization frameworks.

* Corresponding author.
E-mail address: jiahui_yang@berkeley.edu (J. Yang).

https://doi.org/10.1016/j.energy.2026.141111
Received 23 November 2025; Received in revised form 29 March 2026; Accepted 19 April 2026
Available online 22 April 2026

Nomenclature

Parameters

$\dot{m}_{flow}$	borehole mass flow rate [kg/s]
λ_g	thermal conductivity of the grout [W/m K]
λ_p	thermal conductivity of the U-pipe [W/m K]
λ_s	thermal conductivity of the ground [W/m K]
η_{bf}	Effective thermal resistance of borefield
η_{tec}^{char}	Storage charge efficiency [%]
η_{tec}^{dis}	Storage discharge efficiency [%]
η_{tec}^{rate}	Storage charge/discharge rate [%]
η_{tec}^{sto}	Storage efficiency [%]
$\text{Area}_{hub,tec}^{\text{max}}$	Maximum solar PV area [m^2]
$\text{Cap}_{hub,tec}^{\text{max}}$	Maximum technology capacity [kW]
$\text{Car}_{ec,t}$	Carbon intensity of energy [kg-CO_2/kWh]
$\text{COP}_{tec,ec^{\text{in}},ec^{\text{out}}}$	COP for converting input energy to output energy
H_{bf}	BHE length [m]
life_{tec}	Technology lifetime [years]
N_{bf}	Number of BHEs in the borefield
$\text{P}_{ec,m}^{\text{dchar}}$	Energy demand charge [USD/kW/month]
$\text{P}_{ec,t}^{\text{pur}}$	Energy purchase price [USD/kWh]
$\text{P}_{ec,t}^{\text{sal}}$	Energy sale price [USD/kWh]
$\text{P}_{tec}^{\text{fixOM}}$	Fixed O&M cost of technology [USD]
$\text{P}_{tec}^{\text{fix}}$	Fixed installation cost of technology [USD]
$\text{P}_{tec}^{\text{varOM}}$	Variable O&M cost of technology [USD/kW]
$\text{P}_{tec}^{\text{var}}$	Variable installation cost of technology [USD/kW]
Solar_t	Measured electricity generation of solar PV [kW/m^2]
$g_{bf}(\cdot)$	Precalculated g-function for borefield
r_{in}	inner diameter of the U-pipe [m]
r_{out}	outer diameter of the U-pipe [m]
s_{shank}	shank spacing of the U-pipe [m]
Irate	Interest rate (7%)
M	Sufficiently large positive constant

Sets

Hour_m	Hours in month m
Hub	Energy hubs
T^{day}	Daily timesteps
T^{month}	Monthly timesteps
Tec^{BfHp}	BTES heat pump units
Tec^{Bf}	Borefields
$\text{Tup}^{\text{battery}}$	Tuples linking battery storage with stored energy
Tup^{BfHp}	Tuples linking BTES heat pump with its input and output energies
Tup^{Bf}	Tuples linking BTES heat pump unit with its corresponding borefield
Tup^{conv}	Tuples linking technologies with its corresponding input and output energies
Tup^{h2d}	Tuples linking hour t to corresponding day d
$\text{Tup}^{\text{solar}}$	Tuples linking solar PV with its corresponding output energy
Tup^{tank}	Tuples linking stratified water tank with stored heating and cooling energies
T	Hourly timesteps
$\text{Tec}_{ec}^{\text{con}}$	Technologies that consume energy
$\text{Tec}_{ec}^{\text{gen}}$	Technologies that generate energy
Ec	Energy carriers

Variables

$\Delta q_{bt,d}$	Heat pulse (change in heat transfer rate) [kW]
$Area_{hub,tec}$	Solar PV area [m^2]
$Bin_{hub,tec,d}^{\text{BTES}}$	Binary variable for avoiding simultaneous heating and cooling of BTES
$Bin_{hub,tec}$	Binary variable denoting whether technology is installed
C^{CAPEX}	Annualized capital investment [USD]
C^{Energy}	Energy consumption cost [USD]
C^{OM}	Annual operation and maintenance expense [USD]
C^{Total}	Total annualized cost [USD]
$Cap_{hub,tec}$	Installed capacity of technology tec in hub hub [kW]
CO_2^{Total}	Total annual carbon emissions [kg-CO_2]
$Q_{ec,hub,tec,t}^{\text{con}}$	Energy consumption by technologies [kW]
$Q_{ec,hub,tec,t}^{\text{gen}}$	Energy generation from technologies [kW]
$q_{bf,d}$	Heat transfer rate per unit length [kW/m]
$Q_{ec,hub,t}^{\text{dem}}$	Energy demand [kW]
$Q_{ec,hub,t}^{\text{exp}}$	Energy export [kW]
$Q_{ec,hub,t}^{\text{imp}}$	Energy import [kW]
$S_{hub,tec,t}$	Energy stored [kWh]
$T_{bf,d}^{\text{BTES}}$	Average borehole wall temperature [°C]
t_0	First timestep
t_{end}	Last timestep

To characterize subsurface thermal response, numerical simulation is generally considered the most reliable, as it captures detailed subsurface physics, including layered geology [18] and groundwater flow [19]. However, such methods are constrained by high computational cost, extensive model setup effort, and weak integration with building energy simulation tools [20], thus making them impractical to couple with DES optimization. By contrast, analytical and semi-analytical approaches, most notably the g-function method introduced by Eskilson and Claesson [21,22], are more computationally efficient and remain the most widely adopted. The g-function describes borehole wall temperature variations under a constant heat extraction rate, and combined with the temporal superposition principle, it enables estimation under arbitrary time-varying loads [22,23]. Hellström's thermal resistance theory further extended the approach to account for complex borehole geometries [24,25]. Modern implementations, such as `pygfunction` [26–28] and GHEtool [29], build on these advances to simulate irregular borefield layouts and multi-borehole interactions efficiently. Recent developments have focused on improving computational efficiency, discretization strategies, and large-scale applicability of g-function methods in BTES system modeling [30–32]. The development of g-function methods thus provides an opportunity to represent subsurface dynamics in a simplified, or even linear, form, making them attractive for BTES integration into DES optimization frameworks.

On the other hand, the integration of distributed energy resources into DES design is essential for achieving deep decarbonization [33]. Among various DES optimization algorithms [34], Mixed-Integer Linear

Programming (MILP) is one of the most widely adopted [35–37]. Combined with multi-objective optimization methods and the energy hub concept, MILP enables the determination of optimal DES configurations and analysis of the trade-offs between carbon emissions and capital expenditures (CAPEX) [38–42]. The MILP framework further provides opportunities to integrate diverse energy sources into city-scale analyses. For example, solar thermal energy storage systems have been incorporated into DES to assess the performance of solar energy [43–46]; wind turbine has been included to optimize sizing and evaluate their economic impact [47–49]; pumped-hydro energy storage and hydropower generation have been optimized using MILP to quantify their economic contributions [48,50]. By contrast, the integration of BTES into MILP-based DES optimization remains limited. Existing approaches typically rely on highly simplified representations of subsurface thermal behavior. For example, the BTES system is often modeled as a generic storage model with energy loss [51,52], which may not fully capture the subsurface thermal dynamics. More advanced efforts, such as Banke [53], attempted to couple g-function into MILP but used a monthly timescale, which is too coarse to capture optimal operational strategies, and employed a simple ground temperature constraint rather than a fully integrated thermal response model. The primary obstacle to finer temporal resolution lies in the substantial increase in MILP complexity introduced by coupling the g-function approach.

Horizon decomposition techniques are widely used to reduce the computational burden of MILP optimization [54,55], with the Rolling Horizon (RH) method being one of the most effective. By decomposing the full horizon into smaller sub-horizons and iteratively solving subproblems, RH significantly enhances the tractability of MILP models. Compared with the Typical Day method, which approximates the full horizon by clustering representative load days [56], RH preserves chronological continuity, which is critical for modeling storage technologies, whose states are path-dependent and evolve from one timestep to the next. This explains the widespread application of RH in DES optimization [57–62]. A limitation, however, is that when sub-horizons are too short, RH may fail to capture the dynamics of seasonal storage. To address this, Marquant [40] extended RH with a receding horizon formulation, demonstrating improved performance in seasonal storage balance. Thus, RH provides both a practical means of enhancing solvability and a necessary foundation for developing a general MILP g-function framework applicable to simple and complex DES optimization problems.

To address the gap in integrating BTES into DES optimization, this study proposes a novel MILP framework that directly embeds a physics-based g-function formulation to represent subsurface thermal response. This constitutes the first tractable MILP formulation that captures BTES thermal dynamics with physical fidelity at a daily timescale, enabling more reliable system design and operational analysis than existing simplified approaches. However, incorporating the g-function at this level of detail introduces substantial computational complexity, rendering long-horizon optimization intractable. To overcome this limitation, a Rolling Horizon with Multi-Timescale (RH–MTS) strategy is developed, which significantly reduces problem size while preserving solution quality. This method enables the proposed high-fidelity framework to remain computationally feasible for large-scale, long-horizon DES optimization problems relevant to real-world applications. Accordingly, this study aims to (i) develop and validate the MILP g-function framework for accurate subsurface thermal modeling within DES optimization, (ii) evaluate the RH–MTS method as a computational strategy for large-scale optimization, and (iii) demonstrate the applicability of the proposed approach through a case study of the UC Berkeley campus, quantifying the technical, economic, and environmental impacts of BTES deployment, thereby demonstrating the real-world applicability, scalability, and decision-support value of the proposed approach.

2. The g-function method

2.1. Concept and temporal superposition of the g-function

The concept of the temperature response function, commonly referred to as the g-function, was first introduced by Eskilson and Claesson [21,22]. The g-function is a dimensionless, time-dependent function that describes the variation in borehole wall temperature under a constant heat extraction rate from the ground. To extend the representation from a single borehole heat exchanger (BHE) to a borefield containing multiple BHEs, the g-function was further developed to account for borefield geometry and configuration [63], as expressed in Eq. (1):

$$T_b(t) = T^{\text{ini}} - \frac{q_0}{2\pi\lambda}\, g\left(\frac{t}{t_s}, \frac{r_b}{H}, \frac{B}{H}, \frac{D}{H}\right) \tag{1}$$

where $T_b(t)$ is the average temperature at borehole wall, T^{ini} is undisturbed ground temperature, q_0 is a constant heat extraction or injection rate per unit borehole length, λ is ground thermal conductivity. The dimensionless function $g(\cdot)$ is the g-function of the borefield, determined by time t, characteristic time $t_s = H^2/(9\alpha)$ (α is ground thermal diffusivity), borehole radius r_b, BHE spacing B, BHE length H, and borefield buried depth D. Once the borefield configuration is defined, the g-function can be determined, establishing a linear relationship between $T_b(t)$ and q. This linearity forms the basis for coupling the g-function with the MILP framework.

Since the g-function describes the borehole wall temperature response under a constant heat extraction rate, Claesson [22,23] applied the temporal superposition principle to extend it to variable, piecewise-constant heat rates $q(t)$ defined over N steps. This approach decomposes a time-varying profile into a sequence of incremental heat pulses, each initiated at a specific time step, as expressed in Eq. (2). By applying Eq. (1) to each incremental pulse and aggregating the resulting temperature responses, the overall borehole wall temperature can be obtained [64], as shown in Eq. (3).

$$q(t) = \sum_{n=1}^{N} (q_n - q_{n-1})\mathrm{He}(t - t_{n-1}) \tag{2}$$

$$T_b(t) = T^{\text{ini}} + \sum_{n=1}^{N} \frac{\Delta q_n}{2\pi\lambda}\, g\left(\frac{t - t_{n-1}}{t_s}, \frac{r_b}{H}, \frac{B}{H}, \frac{D}{H}\right) \tag{3}$$

where $\Delta q_n = q_n - q_{n-1}$ is the heat pulse (change in heat rate) at timestep t_n, $\mathrm{He}(t - t_{n-1})$ is the Heaviside step function which equals 0 when $t < t_{n-1}$ and 1 when $t \geq t_{n-1}$. Here, $q(t)$ denotes the heat transfer rate per unit borehole length, with positive values representing heat injection into the ground and negative values representing heat extraction. Accordingly, Eq. (3) features a positive sign, in contrast to the negative sign in Eq. (1) where positive represented extraction. Although this convention differs from Claesson's original formulation, it has become widely adopted in contemporary studies for its improved interpretability. Importantly, the superposition preserves the linearity of the g-function, establishing a linear relationship between average borehole wall temperature of the borefield and heat pulses applied at different time steps.

2.2. Estimation of g-function using `pygfunction`

In this study, `pygfunction`, a Python package developed by Cimmino [27], is used to generate g-functions for various geothermal borefields. The package employs a semi-analytical approach that discretizes each borehole into segments and solves the finite line source (FLS) model numerically to estimate the g-function [26]. For a prescribed unit heat rate applied to the borefield, the transient temperature response along the borehole wall is computed over a range of logarithmically spaced time steps. The resulting dimensionless temperature, referred to as the g-function, represents the relationship between the

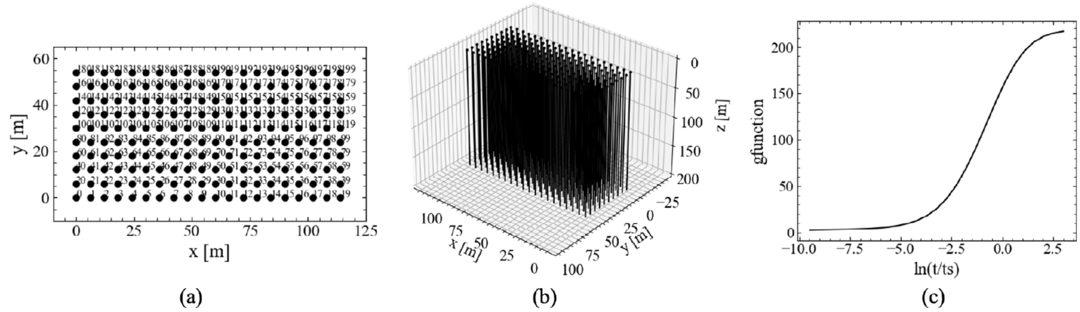

Fig. 1. Rectangular borehole field with 200 vertical boreholes: (a) 2D spatial distribution; (b) 3D visualization; (c) g-function computed using `pygfunction`.

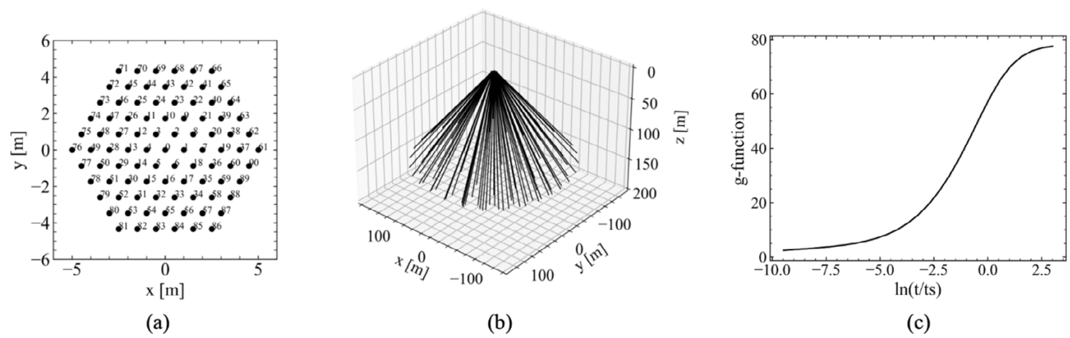

Fig. 2. The drilling platform with 91 inclined boreholes: (a) 2D spatial distribution at the surface; (b) 3D visualization; (c) g-function computed using `pygfunction`.

borefield-average borehole wall temperature variation and the applied heat load.

The calculated g-function depends on both borefield geometry and subsurface thermal parameters, including buried depth, borehole depth, borehole spacing, borehole radius, and ground thermal diffusivity. These parameters determine the magnitude and temporal evolution of the temperature response by governing heat conduction in the surrounding ground and thermal interactions between neighboring boreholes, and are therefore used as inputs to `pygfunction`. Although `pygfunction` does not explicitly capture complex subsurface conditions such as stratification or groundwater flow, it still offers major advantages over finite element models, including lower computational cost, flexible borefield geometry, and simplified setup. It is therefore an efficient and versatile tool for estimating shallow geothermal potential in district-scale energy system optimization. In this work, a ground thermal diffusivity of 9.46×10^{-7} m^2/s, obtained from a campus Thermal Response Test (TRT), is used as the representative value for the UC Berkeley campus site [65], and the same parameter is consistently applied in the g-function generation.

Two borefield configurations are designed to reflect UC Berkeley campus conditions and investigated in this study. The first, shown in Fig. 1, is a conventional vertical field with 20 × 10 BHEs, each 200 m deep and spaced 6 m apart. A single U-pipe is installed in each BHE, and all boreholes are connected in parallel. The resulting g-function is illustrated in Fig. 1(c). The second configuration employs inclined BHEs as shown in Fig. 2. It consists of two inclined platforms, each containing 91 BHEs (90 BHEs arranged in 5 concentric hexagonal rings around a central BHE) with depth of 200 m. Borehole spacing varies from 1 m near the surface to 15 m at the bottom. Each borehole is equipped with a double U-pipe connected in parallel. Due to their compact surface footprint and enhanced thermal performance, inclined borefield are increasingly applied in practice, for instance, the SLB Riboud Product Center in France [66] and the Eversource Framingham project in Boston, USA [67]. The corresponding g-function is shown in Fig. 2(c).

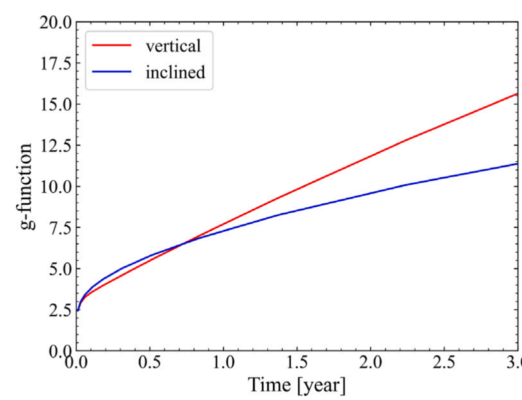

Fig. 3. Comparison of g-functions for borefields with vertical and inclined BHEs over a 3-year time horizon.

Comparison of g-functions in Fig. 1(c) and Fig. 2(c) reveals that borefields with inclined BHEs maintain more stable long-term ground temperatures (roughly 3000 years when $\ln(t/t_s) = 2.5$). A short-term comparison of g-functions is presented in Fig. 3. Initially, the inclined borefield exhibits faster temperature changes due to stronger thermal interactions at shallow depths. After about 0.5 years, however, the vertical borefield shows greater temperature variation as thermal interference among vertical BHEs becomes dominant. By contrast, the inclined borefield stabilizes beyond 0.5 years because the larger spacing at greater depths mitigates thermal interference.

3. Integration of BTES into MILP DES optimization

Optimization of distributed energy system (DES) has become a central strategy for reducing both building energy consumption and carbon emissions. In this section, a general and versatile DES optimization model is formulated using a multi-objective MILP method. The

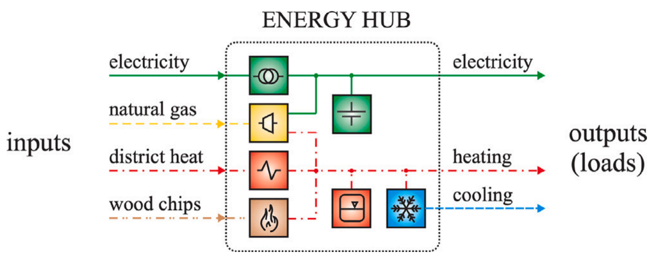

Fig. 4. Energy hub example [70].

concept of the energy hub introduced by Geidl [68–70] is adopted for a flexible and scalable representation of energy flows and conversions in complex multi-energy systems. To better characterize the performance of the subsurface, the g-function method is integrated into the MILP framework. This enables a more accurate representation of subsurface thermal dynamics under heat extraction and injection, thereby supporting a more reliable assessment of shallow geothermal energy potential at multiple scales, with emphasis on the district level.

3.1. The energy hub concept

An energy hub is defined as a unit where multiple energy carriers can be converted, conditioned, and stored [70]. It acts as an interface between energy infrastructures and end-use demands, allowing input energy flows to be transformed into outputs such as heating, cooling, and electricity through various technologies. This abstraction enables complex systems to be modeled in a compact form, facilitating system-level optimization and analysis. Fig. 4 illustrates an example of an energy hub that contains a transformer, a micro turbine, a heat exchanger, a furnace, absorption cooler, a battery, and hot water storage. As a result, the energy hub framework has been widely adopted in DES optimization studies [38–40,44,46].

3.2. Multi-objective MILP for DES optimization

The primary objective of the DES optimization is to minimize both the total system costs and carbon emissions, resulting in a bi-objective formulation with two objective functions in Eq. (4). The cost objective C^{Total} encompasses energy consumption costs C^{Energy}, annualized capital investments C^{CAPEX}, and operation and maintenance expenses (O&M) C^{OM}, while total emissions CO_2^{Total} arise primarily from energy consumption. All cost and emission terms are annualized to ensure consistent comparison across technologies with different lifetimes, scales, and cost structures. Detailed component formulations are provided in Appendix A.1.

$$\min \left\{C^{\text{Total}} = C^{\text{Energy}} + C^{\text{CAPEX}} + C^{\text{OM}}\right\}, \quad \min\, CO_2^{\text{Total}} \tag{4}$$

To solve this bi-objective problem, the Pareto front method [71], which is widely applied in multi-objective optimization [72,73] and DES studies [74–76], is employed. Trade-offs between cost and emissions are explored using the weighted-sum approach, as shown in Eq. (5). By varying the weight $w \in [0,1]$, a set of optimal solutions is generated, forming the Pareto front.

$$\min \left\{w \cdot C^{\text{Total}} + (1-w)\cdot CO_2^{\text{Total}}\right\} \quad \forall\, w \in [0,1] \in \mathbb{R} \tag{5}$$

The formulation of DES MILP models has been extensively reported in the literature [39–42,44,46]. Since the overall DES MILP structure is similar with minor difference depending on research objectives, the detailed MILP-based DES model developed in this study is presented in Appendix, into which the g-function method (Section 3.3) and RH-MTS approach (Section 3.4) are integrated. The formulation primarily consists of: (i) objective functions and components A.1, (ii) the energy balance constraint for each energy carrier A.2, which balancing inflows and outflows at every hub and timestep, and (iii) the representation of energy conversion and storage technologies A.3, which enables transformation between energy carriers.

3.3. Linear constraints of the BTES system

The operation of BTES systems is optimized at a daily instead of hourly scale for three primary considerations: (i) frequent mode switching at short time scales reduces efficiency due to mixing of residual fluid in the BHE, (ii) excessive switching between heating and cooling can shorten the lifetime of heat pump system, and (iii) hourly-scale optimization imposes a heavy computational burden on the MILP framework, as explained in Section 3.3.2. In addition, the flow rate in each borehole pipe is assumed constant. Although real BTES operation involves dynamic flow rates that introduce nonlinearities, this simplification is necessary to preserve MILP tractability.

The BTES constraints consist of two components: a subsurface temperature constraint based on the g-function method (Section 3.3.1) and a reversible heat pump unit (Section 3.3.2). The subsurface temperature constraint captures the relationship between subsurface temperature variation and the heat transfer rate. The reversible heat pump unit converts this heat transfer into usable heating or cooling energy in the network and rescales BTES-related variables from daily to hourly resolution to align with the temporal granularity of the overall optimization model.

3.3.1. The subsurface temperature constraint

The most important feature of BTES is that, the efficiency varies with changes in subsurface temperature during the operation. The heat transfer rate per unit length q_t depends on the temperature difference between the looping fluid and borehole wall thus can be expressed using the thermal resistance theory [24,25] as:

$$q_t \cdot R_b^* = \frac{1}{2}(T_{f,in} + T_{f,out}) - T_b(t) \tag{6}$$

where R_b^* is the effective thermal resistance, which depends on the flow rate, BHE configuration, and thermal properties of the BHE, and $T_{f,in}$ and $T_{f,out}$ are inlet and outlet fluid temperatures. In this study, R_b^* is calculated using the Multipole method [25] implemented in `pygfunction` [77]. Under the constant flow rate assumption, the R_b^* remains constant for each BHE.

Alternatively, the heat transfer rate of a BHE can also be expressed using the energy balance:

$$q_t \cdot H = \dot{m}_{\text{flow}} \cdot c_p \cdot (T_{f,in} - T_{f,out}) \tag{7}$$

where $\dot{m}_{\text{flow}}$ is the flow rate per borehole (assumed constant to preserve linearity), and c_p is the specific heat capacity of looping fluid. Combining Eqs. (6) and (7) yields:

$$q_t \cdot H = \dot{m}_{\text{flow}} \cdot c_p \cdot \eta \cdot \left[T_{f,in} - T_b(t)\right] \tag{8}$$

$$\eta = \frac{2H}{2\dot{m}_f c_p R_b^* + H} \tag{9}$$

where, η is a reduction coefficient characterizing the relationship between the fluid temperature difference, $T_{f,in} - T_{f,out}$, and the fluid-borehole temperature difference, $T_{f,in} - T_b(t)$. Under the constant flow rate assumption, η is constant for each BHE, and consequently, for the entire borefield. Table 1 summarizes the BHE configurations of the vertical and inclined borefields introduced in Section 2.2 along with the effective thermal resistances computed using `pygfunction`. For the vertical borefield with a flow rate of $\dot{m}_{flow} = 0.5$ kg/s per BHE, $\eta = 0.492$. For the inclined borefield with a flow rate of $\dot{m}_{flow} = 1.0$ kg/s per BHE (parallel-connected double U-pipe), $\eta = 0.424$.

Table 1
Configurations of BHEs used in the vertical and inclined borefields and their corresponding effective thermal resistances.

Parameter	Vertical borefield (Single U-pipe)	Inclined borefield (Double U-pipe)
λ_p (W/m K)	0.5	0.5
λ_g (W/m K)	1.6	1.6
λ_s (W/m K)	2.54	2.54
r_{in} (m)	0.016	0.016
r_{out} (m)	0.020	0.020
s_{shank} (m)	0.040	0.060
$\dot{m}_{flow}$ (kg/s)	0.5	1.0
R_b^* (m K/W)	0.147	0.089
η	0.492	0.424

To limit the subsurface temperature variation, the inlet fluid temperature $T_{f,in}$ is constrained within the range $[\mathrm{T}^{\min}_{f,in}, \mathrm{T}^{\max}_{f,in}]$. By reformulating Eqs. (3) and (8) into the MILP framework, the following linear constraints are obtained:

$$\begin{aligned} T^{\mathrm{BTES}}_{bf,d} &= \mathrm{T}^{\mathrm{init}} + \frac{1}{2\pi\lambda} \sum_{n=1}^{N} \Delta q_{bf,d} \cdot g_{bf}\left[(d-n)\cdot \mathrm{He}(d-n)\right] \\ q_{bf,d}\cdot \mathrm{H}_{bf} &= \dot{m}_{\mathrm{flow}} \cdot c_p \cdot \eta_{bf} \cdot \left[T_{f,in} - T^{\mathrm{BTES}}_{bf,d}\right] \\ \mathrm{T}^{\min}_{f,in} &\le T_{f,in} \le \mathrm{T}^{\max}_{f,in} \\ &\forall\, bf \in \mathrm{Tec}^{\mathrm{Bf}},\ d \in \mathrm{T}^{\mathrm{day}} \end{aligned} \tag{10}$$

where N is the number of timesteps in optimization horizon ($N = 365$ for a 1-year optimization), $T^{\min}_{f,in} = 5$°C and $T^{\max}_{f,in} = 30$°C are the assumed inlet fluid temperature bounds in this study, and the g-function is precomputed using `pygfunction`.

3.3.2. The heat pump unit constraint

The reversible heat pump operates in two modes: heating and cooling. In heating mode (ground cooling), it consumes electricity and extracts geothermal energy from the BTES to produce heating (Eq. (11)). In cooling mode (ground heating), it consumes electricity to produce cooling while rejecting geothermal energy to the subsurface (Eq. (12)). Eq. (13) links the heat flow rate of the BHEs to the geothermal energy generated or consumed. Since energy cannot be injected into and extracted from the BTES simultaneously, a binary variable, $Bin^{\mathrm{BTES}}_{hub,tec,d}$, prevents concurrent heating and cooling operation as shown in Eq. (14). Maximum capacity and technology selection are constrained by Eq. (15), consistent with other energy conversion technologies A.3.

$$\begin{aligned} Q^{\mathrm{con}}_{\mathrm{electricity},hub,tec,t} \cdot \mathrm{COP}_{tec,\mathrm{electricity,heating}} &= Q^{\mathrm{gen}}_{\mathrm{heating},hub,tec,t} \\ Q^{\mathrm{con}}_{\mathrm{geo},hub,tec,d} \cdot \mathrm{COP}_{tec,\mathrm{geo,heating}} &= Q^{\mathrm{gen}}_{\mathrm{heating},hub,tec,t} \\ \forall\, hub \in \mathrm{Hub},\ tec \in \mathrm{Tec}^{\mathrm{BfHp}},\ &(t,d) \in \mathrm{Tup}^{\mathrm{h2d}} \end{aligned} \tag{11}$$

$$\begin{aligned} Q^{\mathrm{con}}_{\mathrm{electricity},hub,tec,t} \cdot \mathrm{COP}_{tec,\mathrm{electricity,cooling}} &= Q^{\mathrm{gen}}_{\mathrm{cooling},hub,tec,t} \\ Q^{\mathrm{gen}}_{\mathrm{geo},hub,tec,d} \cdot \mathrm{COP}_{tec,\mathrm{geo,cooling}} &= Q^{\mathrm{gen}}_{\mathrm{cooling},hub,tec,t} \\ \forall\, hub \in \mathrm{Hub},\ tec \in \mathrm{Tec}^{\mathrm{BfHp}},\ &(t,d) \in \mathrm{Tup}^{\mathrm{h2d}} \end{aligned} \tag{12}$$

$$\begin{aligned} Q^{\mathrm{gen}}_{\mathrm{geo},hub,tec,d} - Q^{\mathrm{con}}_{\mathrm{geo},hub,tec,d} &= q_{bf,d} \cdot \mathrm{N}_{bf} \cdot \mathrm{H}_{bf} \\ \forall\, hub \in \mathrm{Hub},\ (tec,bf) \in \mathrm{Tup}^{\mathrm{Bf}},\ &d \in \mathrm{T}^{\mathrm{day}} \end{aligned} \tag{13}$$

$$\begin{aligned} Q^{\mathrm{gen}}_{\mathrm{geo},hub,tec,d} &\le \mathrm{M} \cdot (1 - Bin^{\mathrm{BTES}}_{hub,tec,d}) \\ Q^{\mathrm{con}}_{\mathrm{geo},hub,tec,d} &\le \mathrm{M} \cdot Bin^{\mathrm{BTES}}_{hub,tec,d} \\ \forall\, hub \in \mathrm{Hub},\ tec \in \mathrm{Tec}^{\mathrm{BfHp}},\ &d \in \mathrm{T}^{\mathrm{day}} \end{aligned} \tag{14}$$

$$\begin{aligned} Q^{\mathrm{gen}}_{\mathrm{heating},hub,tec,t} &\le Cap_{hub,tec} \le \mathrm{Cap}^{\max}_{hub,tec} \\ Q^{\mathrm{gen}}_{\mathrm{cooling},hub,tec,t} &\le Cap_{hub,tec} \le \mathrm{Cap}^{\max}_{hub,tec} \\ Cap_{hub,tec} &\le \mathrm{M} \cdot Bin_{hub,tec} \\ \forall\, hub \in \mathrm{Hub},\ (tec, ec^{in}, ec^{out}) &\in \mathrm{Tup}^{\mathrm{BfHp}},\ t \in \mathrm{T} \end{aligned} \tag{15}$$

Eq. (10)–(15) together define the BTES constraints in the MILP framework. These constraints capture subsurface behavior during DES operation but also increase model complexity, primarily due to Eq. (14). This constraint, which prevents simultaneous heating and cooling, requires the introduction of a binary variable, $Bin^{\mathrm{BTES}}_{hub,tec,d}$. This adds 365 daily binaries to a one-year DES optimization; at the hourly scale, the count increases to 8760, making the MILP computationally intractable. This is a key reason why the BTES system is optimized at the daily rather than hourly scale.

3.4. Rolling horizon with multi-timescale (RH-MTS) method

Daily-scale optimization of the BTES module improves the solvability of the MILP model after introducing the g-function. The model remains tractable for one or two BTESs over a one-year horizon, but complexity grows exponentially in larger systems with more BTESs, additional energy hubs, or extended horizons (e.g. 10 years), making full-horizon (FH) optimization computationally prohibitive. To address this, a Rolling Horizon with Multi-Timescale (RH-MTS) method is proposed. Algorithm 1 illustrates the iterative procedure of the RH-MTS method. The hourly full-horizon problem is first decomposed into three sub-horizons: hourly, daily, and monthly. The hourly sub-horizon is optimized directly, while the daily and monthly horizons reduce the number of decision variables, especially binaries. For example, a one-year (8760-hour) problem is reduced to L_{step}+L_{daily}+$L_{monthly}$ timesteps. The model is then solved iteratively by rolling the horizon forward in increments of L_{step} until the full horizon is covered, yielding tractable solutions for complex DES optimization.

Key considerations in implementing the RH-MTS method include timestep aggregation, objective function consistency, and continuity between decomposed models. Average aggregation is employed to cluster the hourly timesteps into daily or monthly intervals. This reduces problem size but may smooth peak demands within the clustered period, leading to deviation from the full-horizon (FH) solution. Objective function consistency is preserved by appending L_{step} timesteps from the following year in each iteration. This ensures a stable balance between energy cost and annualized technology CAPEX. Continuity between decomposed models is maintained by transferring key solution variables from one iteration to the next. Specifically, the final storage state of the previous iteration is used to initialize the next, and capacity variables are treated as minimum constraints in subsequent optimizations.

In addition, the history-dependent behavior of the BTES must be preserved and the lengths of sub-horizons need to be carefully selected. Instead of relying on a single initial state, the cumulative thermal dynamics of the BTES is captured by passing a time series of temperature differences caused by past heat extraction/injection, as illustrated in Fig. 5. Finally, the choice of sub-horizon lengths involves a trade-off: longer L_{step}, shorter L_{daily} and $L_{monthly}$ increase the solution accuracy but also increase the model complexity and solving time, while the opposite setting reduces complexity at the expense of accuracy.

4. Validation of MILP g-function approach

4.1. Modelica model description

To validate the implementation of the g-function within the MILP framework, a benchmark comparison is conducted against a high-fidelity Modelica simulation using the Modelica Buildings Library [78], an open-source platform for simulating building energy systems and district energy systems (DES). The reference Modelica model is based on the reservoir network developed by Sommer [79] and is available in the Modelica Buildings example library. This model serves as a trusted, physics-based baseline for comparison. In Modelica, the BTES system is simulated using the g-function aggregation method, with both short-term and long-term behavior validated against analytical, experimental, and field data [80]. Although based on the same theoretical approach, the Modelica simulation resolves system dynamics in a time-continuous, physics-based manner, providing a high-fidelity benchmark for the MILP g-function framework.

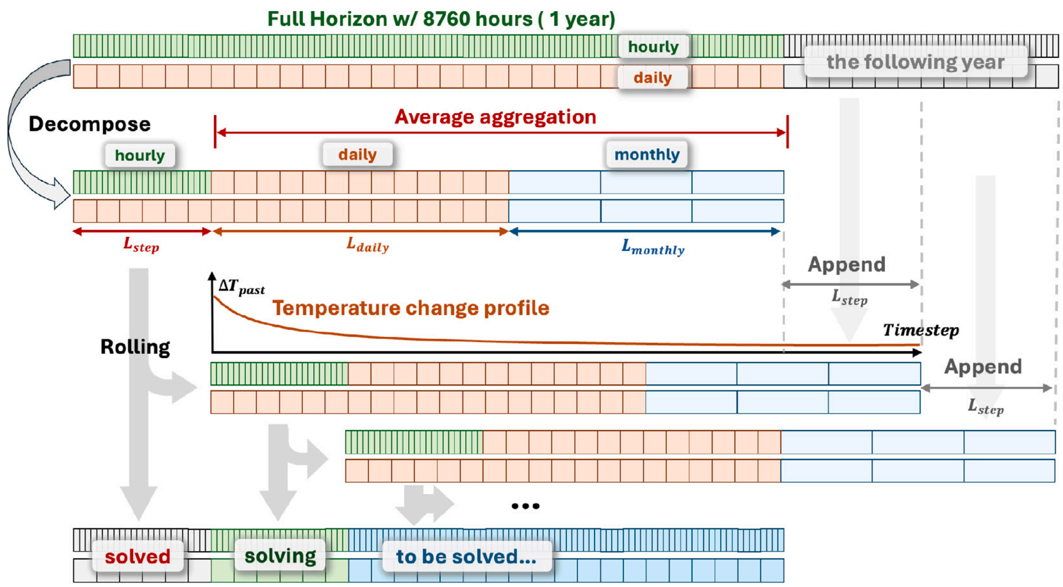

Fig. 5. The Rolling horizon with multi-timescale (RH-MTS) method applied over a one-year period.

Algorithm 1: Iteration procedure for generating Pareto front using the RH-MTS method

---

Result: Pareto front

L_{fh} ← length of full horizon;
L_{step} ← length of hourly sub-horizon;
L_{daily} ← length of daily sub-horizon;
$L_{monthly}$ ← length of monthly sub-horizon;

for *each weight* $w \in [0, 1]$ **do**
  Initialize *State* ← [ ], ΔT_{BTES} ← [ ], *Solution* ← [ ];
  while *True* **do**
    Decompose and aggregate sub-horizons;
    subsolution ← $\min \left[w \cdot C^{\mathrm{Total}} + (1-w) \cdot CO_2^{\mathrm{Total}} \right]$;
    Append *subsolution* to *Solution*;
    if *length(Solution)* < L_{fh} **then**
      Update *State* and ΔT_{BTES};
      Roll horizon and extend by appending L_{step};
    else
      break;
  Export Pareto-optimal solution for current w;
Plot Pareto front curve: Cost vs. CO_2;

The Modelica configuration, shown in Fig. 6, consists of a single-pipe network operating at a constant flow rate, with loop temperatures maintained near ambient conditions. A sewage plant supplies wastewater at 17 °C, acting as either a heat source or sink depending on operating conditions. A borefield with 350 vertical borehole heat exchangers (BHEs), each 300 m deep, is directly connected to the loop. On the demand side, an energy transfer station (ETS) equipped with a space-heating heat pump, a domestic hot water (DHW) heat pump, and a cooling heat exchanger balances the loads. The system serves a Swiss community with annual heating and cooling demands of 3.55 GWh and 0.62 GWh, respectively. Further details are available in [79].

The MILP model is constructed based on this Modelica configuration by reformulating system components into a tractable optimization framework that minimizes electricity consumption, as illustrated in the lower portion of Fig. 6. Detailed specifications of the MILP technologies are provided in Table 2. To ensure comparability between the MILP and Modelica models and to isolate the subsurface thermal response, several simplifications are introduced in the MILP formulation. First, the sewage plant is modeled as an ideal heat source using a heat pump with a sufficiently large COP (denoted as M), reflecting its negligible energy cost under heating-dominated conditions. Second, the thermal network is directly connected to the borefield without intermediate components; a virtual BTES heat pump with negligible cost and COP equal to M is introduced to ensure model feasibility, with a unit energy conversion coefficient. Third, a virtual water tank with hourly resolution is included to maintain operational feasibility under daily BTES operation, while being balanced daily to avoid influencing optimal control decisions.

Table 2
Energy conversion efficiencies of technologies in the MILP model of the constant flow reservoir network.

Technology	Energy conversion		
	Input	Output	COP
Sewage Plant	electricity	net energy	M
BTES Heat Pump	geothermal	net energy	1
	electricity	net energy	M
HeatPump (space heating)	electricity	heating	3
	net energy	heating	1.25
HeatPump (dhw)	electricity	heating	3
	net energy	heating	1.25
WaterEX (cooling)	cooling	net energy	0.95

Notably, the COP of heat pump technologies, including air-source and water-to-water heat pumps, is treated as a constant, as shown in Table 2 of this section and Table 3 of Section 5.3, although it varies with evaporator and condenser temperatures over time. This simplification is adopted to preserve model tractability within the MILP framework and to maintain focus on the proposed MILP g-function method for BTES modeling. A detailed discussion of this assumption is provided in Section 7.1.

4.2. Validation results

Fig. 7 compares the results obtained from the Modelica simulation and the MILP optimization. Two borefields show similar performance, as demonstrated by the average borehole wall temperature in Fig.

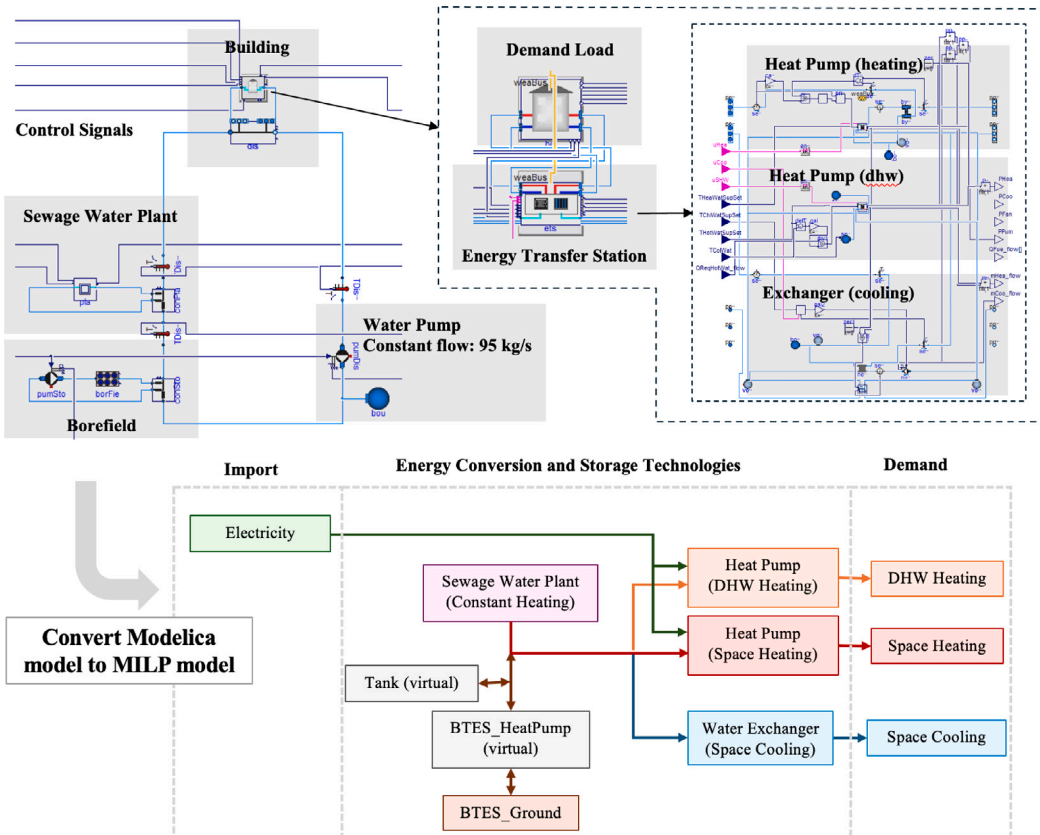

Fig. 6. Modelica configuration of the constant flow reservoir network and the corresponding MILP model configuration.

7(a) and the total energy flow in Fig. 7(b). The borefield's heating contribution is 1.28 GWh in the MILP model with g-function approach, compared to 1.41 GWh in the Modelica simulation. The corresponding cooling contributions are 1.60 GWh (MILP) and 1.56 GWh (Modelica). The borefield energy flow (Fig. 7(b)) from Modelica exhibits larger fluctuations due to its hourly resolution, whereas the MILP results, computed on a daily scale, are smoothed by the virtual water tank introduced in Section 4.1. Given the fundamental differences between the physics-based representation in Modelica and the simplified linear formulation in the MILP model, these discrepancies are considered acceptable.

Fig. 7(c) presents the energy flow from the sewage water plant. Here, notable differences in temporal patterns can be observed between the two models, primarily due to the virtual tank in the MILP formulation. This tank is used to ensure consistency between daily BTES operation and the hourly resolution of the optimization model. It acts as a buffer that balances energy flows within each day without affecting the underlying subsurface thermal response. Despite these variations, the total heating energy is nearly identical: 2.06 GWh in the Modelica simulation and 2.07 GWh in the MILP optimization. Therefore, the discrepancy is primarily due to modeling simplifications required for tractability and does not affect the overall energy balance or the validity of the MILP g-function method.

In general, the MILP g-function approach exhibits performance comparable to that of the Modelica simulation in estimating borefield temperature and energy flow. While the Modelica simulation provides a higher-fidelity representation by accounting for detailed physical processes, the close agreement between the two approaches confirms that the MILP formulation captures the key subsurface thermal dynamics with sufficient accuracy for optimization purposes.

5. Case study description

5.1. UC Berkeley clean energy campus plan

The UC Berkeley main campus currently relies on a century-old cogeneration heating plant comprising a gas turbine and four gas boilers that supply both campus electricity and steam. This system emits over 10,000 tons of CO_2 annually, about 80% of the campus's total carbon emissions, and experiences substantial energy losses due to infrastructure degradation (15% thermal mass loss and 20% heat transfer loss). To address these challenges, the campus has initiated the Clean Energy Campus (CEC) plan, aiming to replace the aging plant with an electrified heating and cooling plant (EHCP) and achieve an 85% carbon reduction by 2035 [81]. The EHCP discussed in this study incorporates heat recovery chillers, cooling towers, electric boilers, a stratified thermal energy storage tank, and Borehole Thermal Energy Storage (BTES), supported by a new distribution network and building-side system conversions.

5.2. Demand profile generation

Building energy consumption data, including electricity, space heating, space cooling, and domestic hot water heating, were generated using EnergyPlus and calibrated with measured data. Campus buildings were grouped into five categories (office, datacenter, laboratory, classroom, and residence; Fig. 8 a), each represented by an archetype model (midsize office, data center, laboratory, college, and midsize apartment). Operational schedules were modified in OpenStudio to reflect Berkeley-specific use patterns, and weather data from Oakland International Airport were applied. Energy use of individual buildings was estimated by scaling prototype outputs by floor area. Calibration employed measured electricity (roughly 80% coverage) and steam data (roughly 30% coverage) from 2019, the last pre-pandemic year with

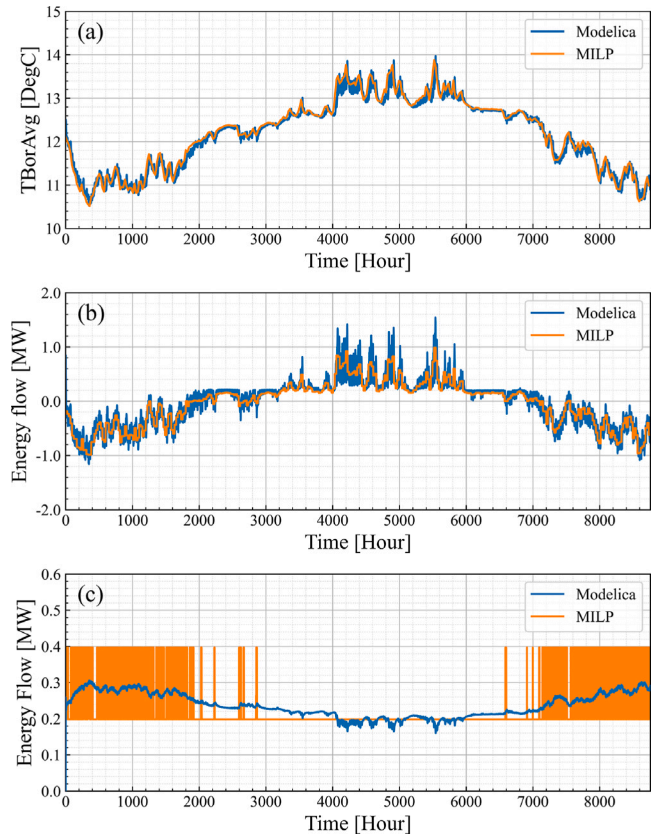

Fig. 7. Comparison of results from Modelica simulation and MILP optimization: (a) Average borehole wall temperature of the borefield; (b) Total energy flow supplied from the borefield; (c) Total energy flow supplied from the sewage water plant.

stable operations. Limited steam coverage reflects the age of campus infrastructure, with many buildings lacking reliable meters. Total campus energy demand was obtained by aggregating building-level consumption shown in Fig. 8(b). The resulting annual heating demand (space heating + domestic hot water) is 148 GWh, consistent with the 150 GWh effective heating delivered by the present cogeneration plant after accounting for steam delivery loss and building-side conversion loss [82] and 154 GWh estimated by a consulting company [81]. Annual cooling demand is estimated at 142 GWh, closely aligned with the consultant's estimate of 135 GWh [81], supporting the validity of the simulation results.

5.3. Configuration of the MILP model

Fig. 9 illustrates the configuration of the MILP optimization model, which simplifies the UC Berkeley main campus into a single energy hub, with energy imports, conversion technologies, and demand organized from left to right. The gray-shaded area represents the existing cogeneration system, consisting of a gas turbine and boilers that produce steam and electricity. Steam is distributed through the steam network and converted to space heating and domestic hot water heating by building exchangers. The system prioritizes steam supply while also generating roughly 90% of total electricity demand; the remainder of electricity comes from solar PV and the utility grid. Cooling demand is currently met by building chillers. The green-shaded area in Fig. 9 depicts the planned EHCP system which includes a heat recovery pump, stratified water thermal energy storage, and two BTES systems (vertical and inclined fields). An electric boiler supplements heating, while an ASHP and cooling tower add cooling capacity. Expanded solar PV and battery storage improve flexibility. A new water-based distribution network (54–72 °C for heating, 5–13 °C for cooling) will replace the steam network. On the building side, water-to-water exchangers are installed to comply with the distribution system.

Dynamic electricity rate and carbon intensity in California are considered. The PG&E B20 time-of-use (TOU) tariff (shown in Fig. 10(a)) is applied with a demand charge of 37.86 USD/kW/month [83]. Carbon intensity follows 2023 marginal emission rates from CARB as shown in Fig. 10(b) [84]. Due to the substantial contribution of solar PV in California, the carbon intensity is lower during the daytime and higher at night. Natural gas costs 0.064 USD/kWh with a 10 USD/kW/month demand charge and emits 0.181 kg-CO_2/kWh. Technology specifications and linearized costs are summarized in Tables 3–4. BTES includes a heat pump unit listed in Table 3 and the corresponding borefield unit listed in Table 4. The cost of borehole drilling is assumed fixed at 20,000 USD for drilling a vertical borehole with a depth of 700 ft (213 m) and 30,000 USD for drilling an inclined borehole with a depth of 700 ft (213 m). The resulting costs of two borefields in Section 2.2 are 4,000,000 USD and 5,490,000 USD, respectively. The O&M cost of the borehole is assumed negligible due to low maintenance of underground structures.

6. Results

The campus DES was optimized with the MILP g-function model under three scenarios: (i) one-year optimization with the FH method (1-year FH), (ii) one-year optimization with the RH-MTS method (1-year RH-MTS), and (iii) ten-year optimization with the RH-MTS method (10-year RH-MTS). The resulting Pareto fronts are shown in Fig. 11, where the 1-year FH solutions (red diamond markers) serve as the baseline for evaluating the transition pathway and assessing RH-MTS performance. Four representative solutions (1, 2, 4, and 6), highlighted with red dashed circles, are selected for detailed analysis. The corresponding utilized capacities are listed in Table 5, and the marginal abatement cost of each transition is provided in Table 6.

6.1. Campus DES transition under the 1-year FH scenario

The 1-year FH results are shown as red diamond markers in Fig. 11, with corresponding technology capacities listed in Table 5. Pareto_1, which minimizes the total cost, essentially reflects the current campus energy system, except that additional solar PV and a battery are installed to eliminate imported electricity (currently 10 % of campus consumption). This solution yields annual carbon emissions of 122,473 tons, close to the 120,000 tons reported by UC Berkeley [81], and an annualized cost of 78.5 million USD, dominated by natural gas purchases, cogeneration operation, and steam network maintenance. In Pareto_2, all steam-based technologies are replaced with the new EHCP system, and imported electricity becomes the primary energy and emissions source. This transition reduces carbon emissions by 40% (to 71,755 tons) at a marginal abatement cost of 64 USD/ton, consistent with the decarbonization pathway currently pursued by UC Berkeley.

Further carbon reductions from Pareto_2 to Pareto_6 are achieved by expanding new technologies, particularly storage. With natural gas phased out, emissions originate primarily from electricity use. Electricity demand decreases slightly (by 3 GWh) from Pareto_2 to Pareto_4 and then stabilizes, while average electricity prices rise and average carbon intensity declines, as shown in Fig. 12. In California, daytime electricity prices are higher due to peak demand, yet carbon intensity is lower because of widespread solar PV generation (Fig. 10). The MILP model therefore shifts electricity imports to daytime hours to reduce emissions at the expense of higher costs. Consequently, the marginal abatement cost increases from 303 USD/ton (Pareto_1 to Pareto_4) to 563 USD/ton (Pareto_1 to Pareto_6), as indicated in Table 6. Considering this trade-off, Pareto_4 is considered as the most cost-effective solution for the Berkeley campus and is selected for further analysis in this study.

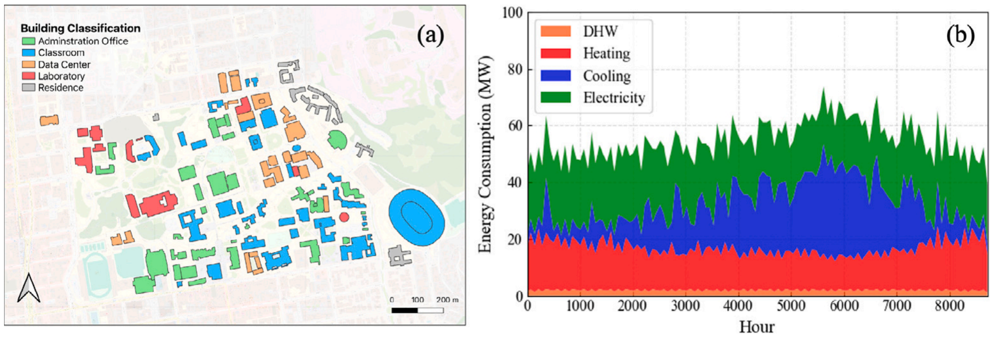

Fig. 8. UC Berkeley main campus: (a) building classification by use type; (b) total energy consumption of the main campus, resampled over a 3-day interval for better visualization.

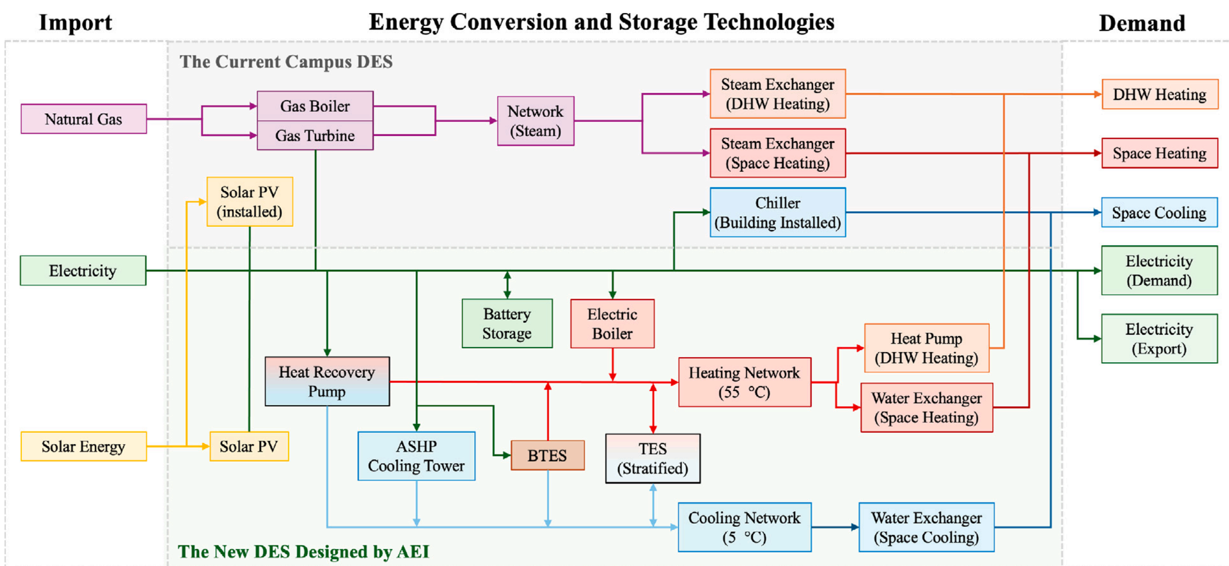

Fig. 9. MILP configuration for the Berkeley main campus case study. The campus is generalized as a single energy hub. The diagram illustrates the energy system structure from left to right: energy import, energy conversion and storage technologies, and energy demand.

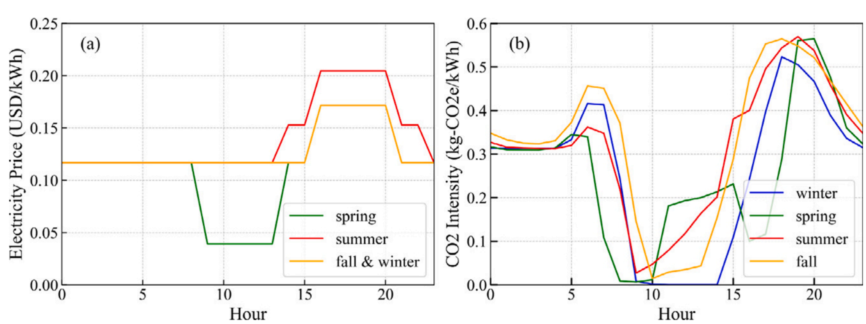

Fig. 10. Dynamic profiles of electricity price and carbon intensity in California: (a) PG&E B20 time-of-use rate schedule; (b) typical hourly carbon emission factors associated with grid electricity.

6.2. BTES performance under the 1-year FH scenario

As shown in Table 5, both vertical and inclined borefields, together with their heat pumps, are first selected in Pareto_2, indicating that BTES is a cost-effective option for reducing cost and emissions. In Pareto_4, the installed heat pump capacities reach 2025 kW for the vertical borefield and 2503 kW for the inclined borefield. The larger capacity of the inclined field reflects the enhanced heat transfer efficiency of the double U-pipe configuration. The operational performance of both systems under the 1-year FH scenario is shown in Fig. 13 (a, c), including four phases: ground cooling (building heating), mode switching, ground heating (building cooling), and a subsequent ground cooling phase.

During the initial ground cooling phase, the average borehole wall temperature (TBorAvg) (Fig. 13(a)) decreases toward the minimum inlet temperature for ground cooling (5 °C as represented by blue dashed line). Initial heating energy flows are 2025 kW (vertical) and 2503 kW (inclined) as summarized in Table 7, but both decline as the difference between TBorAvg and the minimum inlet temperature narrows. The maximum allowable heat transfer rate constrained by Eq. (10) therefore decreases. By the end of this three-month phase, both heating energy flows fall to roughly 1310 kW, corresponding to

Table 3
Technical specifications and cost parameters of energy conversion technologies used in the system.

Technology	Energy conversion			Capacity		Cost		O&M		Life time
	Input	Output	COP	Installed (kW)	Max (kW)	Fixed (USD)	Variable (USD/kW)	Fixed (USD)	Variable (USD/kW)	Years
Gas Turbine	natural gas	steam	0.41	30,000	–	100	0	2,750,000	0	10
		electricity	0.28	–	–	–	–	–	–	–
Gas Boiler	natural gas	steam	0.77	40,000	–	100	0	1,750,000	0	10
Steam Network	steam	steam	0.65	60,000	–	100	0	3,250,000	0	10
SteamEX (heating)	steam	space heating	0.95	60,000	–	100	0	1000	4	10
SteamEX (DHW)	steam	DHW heating	0.95	7000	–	100	0	1000	4	10
Chiller (installed)	electricity	space cooling	3.5	25,000	–	100	0	1000	4	10
Solar PV (installed)	solar	electricity	1	446	–	100	0	1000	2	30
Heat Recovery Pump	electricity	heating	4	–	100,000	100	700	1000	12	30
		cooling	3	–	–	–	–	–	–	–
BTES Heat Pump	electricity	heating	7	–	10,000	100	700	1000	12	30
		cooling	6	–	–	–	–	–	–	–
ASHP (cooling)	electricity	cooling	3	–	–	100	1500	100	10	30
Cooling Tower	electricity	cooling	5	–	–	10,000	50	100	6	30
Electric Boiler	electricity	heating	0.99	–	–	100	100	100	2	30
HeatPump (DHW)	electricity	heating	3	–	–	100	700	1000	12	30
WaterEX (cooling)	cooling	cooling	0.95	–	–	100	500	100	4	30
WaterEX (heating)	heating	heating	0.95	–	–	100	500	100	4	30
Solar PV	solar	electricity	1		2000	100	0	1000	2	30
Heating Network	heating	heating	0.96	–	–	120,000,000	0	500,000	0	80
Cooling Network	cooling	cooling	0.98	–	–	120,000,000	0	500,000	0	80

Table 4
Technical specifications and cost parameters of energy storage technologies used in the system.

Technology	Energy stored	Capacity		Cost		O&M		Life time
		Installed (kWh)	Max (kWh)	Fixed (USD)	Variable (USD/kWh)	Fixed (USD/year)	Variable (USD/kWh/year)	Years
Stratified Water Tank	heating/cooling	–	400,000	10,000	50	10,000	0.5	50
Battery	electricity	–	100,000	10,000	300	10,000	1.5	30
Borehole Field (vertical)	geothermal	–	–	4,000,000	0	200	0	80
Borehole Field (inclined)	geothermal	–	–	5,460,000	0	200	0	80

Table 5
Utilized capacities of technologies in each Pareto-optimal solution. Energy conversion technologies are expressed in kW, and energy storage technologies in kWh. For borefields, a value of 0 indicates not installed, while 1 indicates installed.

Technology	Pareto_1			Pareto_2			Pareto_4			Pareto_6		
	FH [1 year]	RH-MTS [1 year]	RH-MTS [10 years]	FH [1 year]	RH-MTS [1 year]	RH-MTS [10 years]	FH [1 year]	RH-MTS [1 year]	RH-MTS [10 years]	FH [1 year]	RH-MTS [1 year]	RH-MTS [10 years]
Gas Turbine	40,000	40,000	40,000	0	0	0	0	0	0	0	0	0
Gas Boiler	50,000	50,000	50,000	0	0	0	0	0	0	0	0	0
Steam Network	52,518	52,518	58,012	0	0	0	0	0	0	0	0	0
SteamEX (heating)	44,266	44,266	48,897	0	0	0	0	0	0	0	0	0
SteamEX (DHW)	6310	6310	6901	0	0	0	0	0	0	0	0	0
Chiller (installed)	76,931	76,931	84,672	52,125	52,427	54,934	33,289	45,376	47,697	0	0	0
Solar PV (installed)	5200	5200	5200	5200	5200	5200	5200	5200	5200	5200	5200	5200
HeatPump Recovery	0	0	0	24,580	22,262	24,494	28,826	26,877	29,196	60,927	60,429	66,397
HeatPump BTES_V	0	0	0	1778	2830	3073	2025	3198	3199	2645	3251	3370
HeatPump BTES_I	0	0	0	2159	3734	4018	2503	4028	4130	3690	4093	4330
ASHP (cooling)	0	0	0	0	0	0	0	0	0	0	0	0
Cooling Tower	0	0	0	0	14,609	18,301	23,390	22,496	23,629	99,208	102,641	112,765
Electric Boiler	0	0	0	17,182	22,241	27,182	37,851	37,564	43,073	84,690	103,484	107,084
HeatPump (DHW)	0	0	0	6310	6310	6901	6310	6310	6901	6310	6310	6901
WaterEX (heating)	0	0	0	44,266	44,266	48,897	44,266	44,266	48,897	44,266	44,266	48,897
WaterEX (cooling)	0	0	0	24,806	25,536	29,738	43,642	32,528	36,976	76,931	76,931	84,672
Solar PV	20,000	20,000	20,000	20,000	20,000	20,000	20,000	20,000	20,000	20,000	20,000	20,000
Heating Network	0	0	0	50,346	50,346	55,614	50,346	50,346	55,614	50,346	50,346	55,614
Cooling Network	0	0	0	26,112	26,880	31,303	45,939	34,240	38,922	80,980	80,980	89,128
Strafied Water Tank	0	0	0	143,764	198,428	257,929	284,251	309,747	400,000	400,000	400,000	400,000
Battery	63,494	27,260	33,786	68,939	15,091	19,905	100,000	100,000	100,000	100,000	100,000	100,000
Borefield (vertical)	0	0	0	1	1	1	1	1	1	1	1	1
Borefield (inclined)	0	0	0	1	1	1	1	1	1	1	1	1

Table 6
Marginal abatement costs of transitions from Pareto_1 (similar to the current campus DES) to other solutions [USD/ton-CO_2].

Transition	FH [1 year]	RH-MTS [1 year]	RH-MTS [10 years]
Pareto_1 to Pareto_2	63	86	33
Pareto_1 to Pareto_4	302	299	265
Pareto_1 to Pareto_6	563	573	616

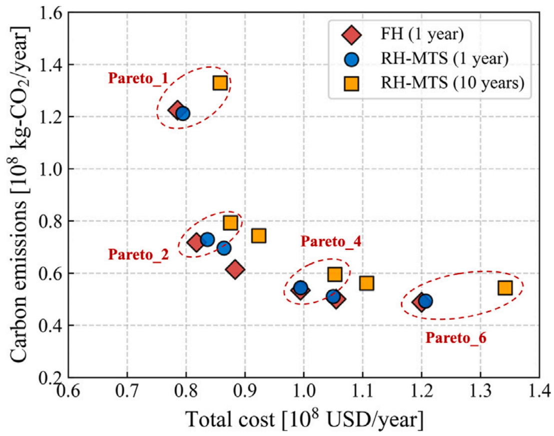

Fig. 11. Pareto-optimal solutions obtained under different optimization scenarios. Solutions 1, 2, 4, and 6, highlighted by the red dashed circle, are selected for further analysis.

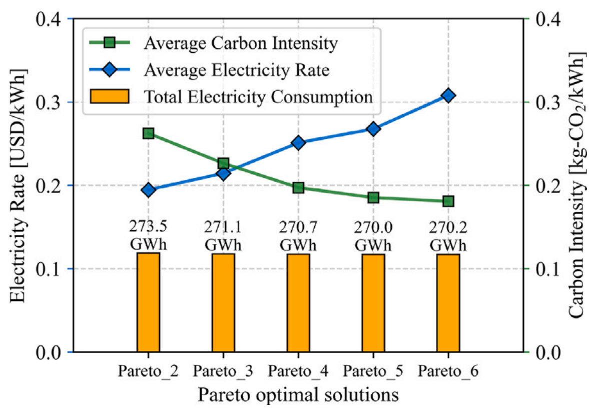

Fig. 12. Total annual electricity consumption and the corresponding average rate and carbon emission intensity in each Pareto-optimal solution under the 1-year FH scenario.

reductions of 36% (vertical) and 48% (inclined). The inclined borefield shows faster decline due to higher transfer efficiency. During the switching phase, frequent mode changes temporarily increase the energy flows (Fig. 13(c)), as switching between modes shortly raises the temperature difference between inlet fluid and TBorAvg, widening the thermal gradient. Entering the ground heating season, both borefields show similar decline trends: cooling energy flows start at 1687 kW (vertical) and 2085 kW (inclined) but drop to roughly 790 kW after five months, corresponding to reductions of 54% and 63%. In the second cooling phase, elevated borefield temperatures initially limit flows by heat pump capacity, but within 10 days flow declines again as the gradient diminishes.

Table 8 compares the total energy supply, average energy price, and carbon intensity of vertical and inclined borefields against other technologies. The vertical borefield supplies 5.4 GWh of heating and 4.6 GWh of cooling energy annually, while the inclined borefield provides 6.6 GWh and 4.8 GWh of heating and cooling, respectively. Despite greater output, the inclined borefield has a higher average cost (0.077 USD/kWh vs. 0.070 USD/kWh) due to more expensive drilling and installation costs (30,000 USD per inclined vs. 20,000 USD per vertical borehole). Thus, its primary advantage lies in space efficiency rather than economics. Both borefields yield the same average carbon intensity of 0.054 kg-CO_2/kWh, since identical heat pump COPs are used. Among alternatives, the heat recovery pump achieves the lowest cost, followed by the cooling tower due to its high COP, while the electric boiler shows both the highest cost and highest carbon intensity.

Overall, the MILP with the g-function approach effectively models BTES performance, capturing both the ground temperature response and the decline of borefield energy supply over time. This framework enables robust comparisons between borefield configurations and alternative technologies, supporting more reliable system design and planning.

6.3. Assessment of the RH-MTS method

In the 1-year RH-MTS scenario, lengths of hourly, daily, and monthly sub-horizons are set to 2160, 150, and 3, respectively. Solving six Pareto-optimal solutions with the Gurobi solver on an Intel Xeon w7-2495X CPU required 0.5 h, compared with 1.9 h for the 1-year FH scenario, a 73% reduction in computational time. While the present case study is relatively simple, even greater savings are expected for larger systems with multiple energy hubs, more BTES, or longer horizons.

Fig. 11 shows that the Pareto fronts from RH-MTS and FH are highly consistent, with some solutions (e.g., Pareto_1 and Pareto_4–6) being identical. 1-year RH-MTS results are generally shifted slightly toward higher costs and emissions, indicating minor losses in optimality. Marginal abatement costs are also consistent: from Pareto_1 to Pareto_2, Pareto_4, and Pareto_6, the values are 86 USD/ton, 299 USD/ton, and 573 USD/ton, respectively, corresponding to deviations of +34.4%, −1.3%, and −1.8% compared with the 1-year FH results (Table 6). Utilized capacities (Table 5) show RH-MTS slightly underestimates heat recovery pump size but overestimates others due to averaging when clustering hourly variables into daily or monthly ones.

The RH-MTS method also preserves the cyclic patterns and continuity of storage technologies in spite of horizon decomposition. Fig. 14 compares energy stored in the stratified water tank under both approaches, showing that operational patterns are accurately replicated. No storage is used in cost-minimized cases; in Pareto_2, a small tank smooths short-term fluctuations, while in carbon-prioritized cases, tank size grows to the maximum 400 MWh to balance loads over a longer period.

BTES performance under RH-MTS (Fig. 13 (b, d)) closely resembles FH results, with similar seasonal shifts and gradual declines in energy flow. Minor differences appear in fluctuations: FH predicts more variation during cooling phases, while RH-MTS shows more during switching periods, occasionally leading to simultaneous heating and cooling across borefields due to underestimated heat recovery capacity. RH-MTS also predicts higher peak heating and cooling flows and correspondingly larger heat pump capacities, producing more pronounced declines, yet residual flows converge with FH results. Importantly, total annual heating and cooling supplies are nearly identical: 5.6 GWh and 7.0 GWh (RH-MTS) versus 5.4 GWh and 6.6 GWh (FH) for heating, and 4.9 GWh and 4.8 GWh versus 4.6 GWh and 4.9 GWh for cooling. Deviations remain within 6%, acceptable given the large computational savings.

Overall, these results demonstrate that the RH-MTS method can reproduce the Pareto front with high fidelity while substantially reducing solution time, making it a practical approach for large-scale and complex multi-objective optimization problems.

6.4. Long-term performance of BTES system

The long-term performance of BTES systems has been a major concern, as efficiency often degrades after several years of operation. The 1-year optimization presented earlier does not capture these effects. By year-end, the changed ground temperature (Fig. 13 (a, b)) suggests that subsurface condition and energy supply will differ in subsequent years. To address this, a 10-year optimization was conducted using the RH-MTS method, with a demand scaling factor of 1.01 to reflect 1%

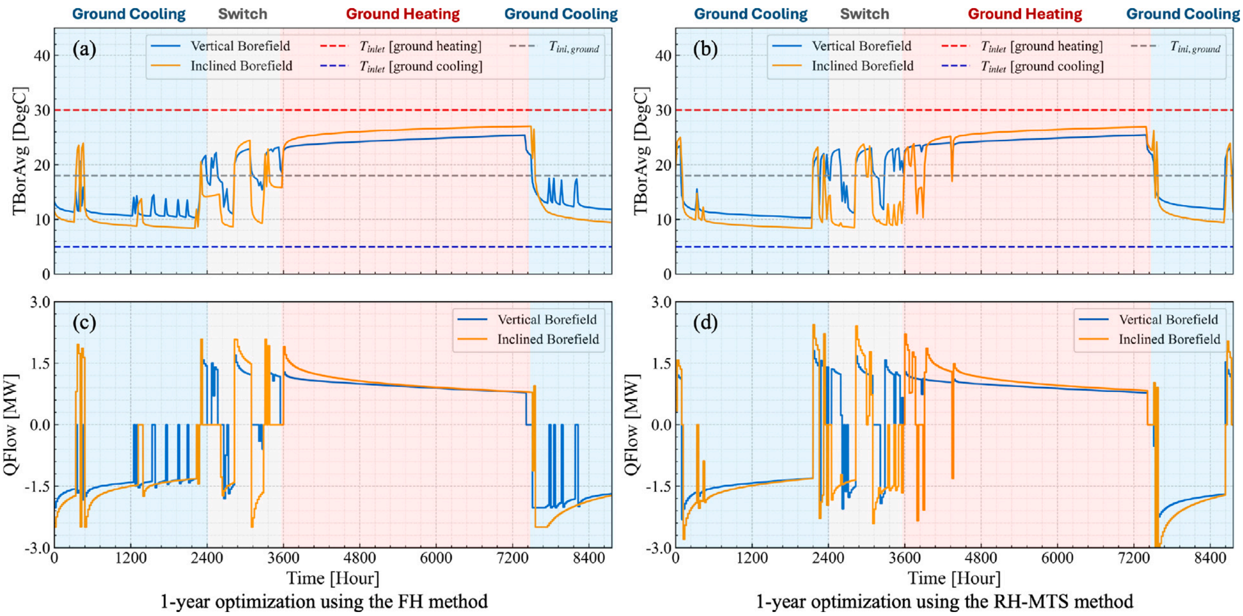

Fig. 13. Performance of the BTES systems under different optimization scenarios: (a, b) average borehole wall temperature (TBorAvg) udner the 1-year FH and 1-year RH-MTS scenarios, where the red and blue dashed lines denote the maximum and minimum inlet fluid temperatures, respectively, and the gray dashed line denotes the initial ground temperature; (c, d) total energy flow of the BTES systems under the 1-year FH and 1-year RH-MTS scenarios, where negative values indicate heat extraction from the ground (heating supply) and positive values indicate heat injection into the ground (cooling supply).

Table 7
Decline in energy flow from borefields under the 1-year FH and 1-year RH-MTS scenarios.

	1-year FH		1-year RH-MTS	
	Inclined borefield	Vertical borefield	Inclined borefield	Vertical borefield
Peak Heating [kW]	2025	2503	2538	3461
Residual Heating [kW]	1310	1317	1303	1312
Heating Decline	36%	48%	49%	63%
Peak Cooling [kW]	1687	2085	1802	2433
Residual Cooling [kW]	786	793	779	832
Cooling Decline	54%	63%	57%	66%

Table 8
Comparison of energy supply, average energy price, and average carbon intensity for the heat recovery pump, vertical borefield, inclined borefield, cooling tower, and electric boiler.

	Vertical borefield	Inclined borefield	Heat recovery pump	Cooling tower	Electric boiler
Heating [GWh]	5.4	6.6	117.9	–	25.3
Cooling [GWh]	4.6	4.8	88.4	42.7	–
Total Energy Supply [GWh]	10.0	11.3	206.4	42.7	25.3
Annualized CAPEX [USD]	436,563	581,162	1,626,074	94,326	305,029
Annualized O&M [USD]	25,295	31,027	346,907	140,439	75,710
Electricity Cost [USD]	233,006	263,437	4,053,840	1,090,922	2,854,372
Carbon Emissions [tons]	537	608	9709	2014	2293
Average Energy Cost [USD/kWh]	0.070	0.077	0.029	0.031	0.128
Average Energy Carbon Intensity [kg-co2/kWh]	0.054	0.054	0.047	0.047	0.091

Table 9
Total annual heating and cooling supply from borefields under three different scenarios.

		1-year FH	1-year RH-MTS	10-year RH-MTS		
				1st year	5th year	Average (year 5 to 10)
Vertical Borefield	Heating [GWh]	5.39	5.56	5.56	6.17	6.16
	Cooling [GWh]	4.56	4.92	4.92	4.25	4.31
Inclined Borefield	Heating [GWh]	6.56	6.98	6.98	6.54	6.64
	Cooling [GWh]	4.78	4.86	4.86	4.62	4.68

annual demand growth (10.5% increase after 10 years). The RH-MTS model was solved in 2.5 h, whereas the FH method proved infeasible due to a tenfold increase in variables, particularly binaries, which caused exponential growth in solution time. The Pareto front of the 10-year RH-MTS scenario is shown as orange square markers in Fig. 11. Reported carbon emissions and annualized costs represent averages

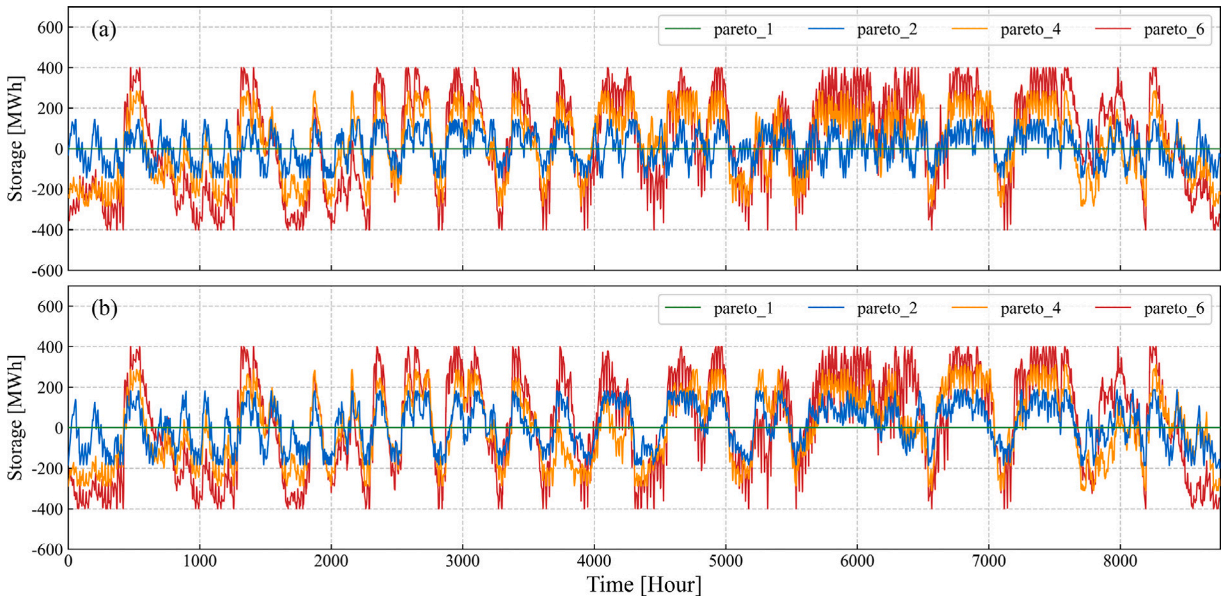

Fig. 14. Variation of energy stored in the stratified water tank over time in different Pareto-optimal solutions: (a) the 1-year FH scenario; (b) the 1-year RH-MTS scenario.

over the horizon (10 years). As expected, the Pareto front shifts upward and to the right relative to 1-year FH results, reflecting both increased energy demand and higher technology capacities: the higher carbon emissions result directly from the additional demand, whereas the higher costs reflect a combination of increased energy purchases and the larger technology capacities required.

Long-term BTES performance is illustrated in Fig. 15. Seasonal operating patterns remain consistent with the 1-year case, but over time the ground temperature stabilizes between the inlet fluid temperature bounds. Annual energy supply (Fig. 16) shows that the vertical borefield delivers on average 6.0 GWh heating (±0.5 GWh) and 4.4 GWh cooling (±0.5 GWh) per year, while the inclined borefield performs slightly better at 6.7 GWh heating (±0.3 GWh) and 4.7 GWh cooling (±0.2 GWh). Despite rising demand, borefield contributions remain stable, indicating that BTES is fully utilized and cannot accommodate additional demand growth. Performance varies most in the first four years. For example, annual heating of vertical borefield increases from 5.56 to 6.26 GWh (+12.3%), while annual cooling decreases from 4.9 to 4.3 GWh (−12.2%). This behavior is primarily influenced by system settings, including initial ground temperature, temperature bounds of inlet fluid, and BTES start-up timing, and is discussed further in Section 7.2. After 4 years, both borefields reach stable operation with only minor year-to-year variation. Table 9 compares annual energy supply of borefields under different scenarios. The first-year results of the 10-year RH-MTS scenario match those of the 1-year RH-MTS case (differences within the kWh range). This occurs because the optimization in the first year follows a similar procedure for two scenarios: while the 10-year RH-MTS formulation accounts for future demand over the next nine years, this demand is aggregated at the monthly level. Since the campus heating and cooling loads are relatively balanced, the influence of future demand largely cancels out and has little effect on the first-year results. In subsequent years, however, the effect of ground temperature changes carried over from previous years must be considered, leading to adjustments in the annual energy supply. After stabilization, the average annual heating and cooling supply may deviate by up to 12% from the first-year values, depending on the specific BTES system settings.

7. Discussion

7.1. The constant COP assumption for heat pumps

The assumption of a constant COP for heat pump technologies (e.g. water-to-water and air-source heat pumps) represents a simplification that introduces certain limitations, as heat pump performance is known to vary with the condenser and evaporator temperatures. Although temperature-dependent COP relationships can be incorporated into MILP using linear approximations, such formulations require additional validation due to the lack of well-established models. Therefore, a constant annual-average COP is adopted. This simplification is consistent with the objective of identifying optimal technology combinations rather than precisely modeling individual technology performance, and it facilitates a clearer evaluation of the proposed MILP-based g-function method for BTES modeling. Although empirical COP curves could be used to approximate performance variations, such approaches require high-quality, site-specific operational data, which are not available for the UC Berkeley campus; therefore, average COP values provided by the campus are used. Furthermore, this study is conducted within a platform-based design (PBD) framework [38], in which simplified energy models are employed at the system optimization stage, followed by higher-fidelity, physics-based simulations (e.g., using the Modelica Buildings Library) to capture detailed performance such as COP variation. Any discrepancies identified at the high-fidelity stage can be used to iteratively refine the system-level optimization (e.g. modifying COP), ensuring both computational efficiency and modeling accuracy.

7.2. Limitations of the MILP g-function method

The integration of BTES into MILP requires linearity assumptions of constant flow rate and fixed inlet temperatures, which introduce the limitations and directly affect the BTES performance. For the UC Berkeley case, the initial ground temperature is 18 °C, with inlet temperatures bound of [5, 30] °C, yielding average specific extraction rates of 31.5 W/m (vertical) and 35.0 W/m (inclined). Raising the upper bound of the inlet fluid temperature to 50 °C increases these values to 51.6 W/m and 56.6 W/m, respectively, and the first four years also show more significant redistribution effects as the ground adjusts between 5–50 °C, boosting heating but reducing cooling supply.

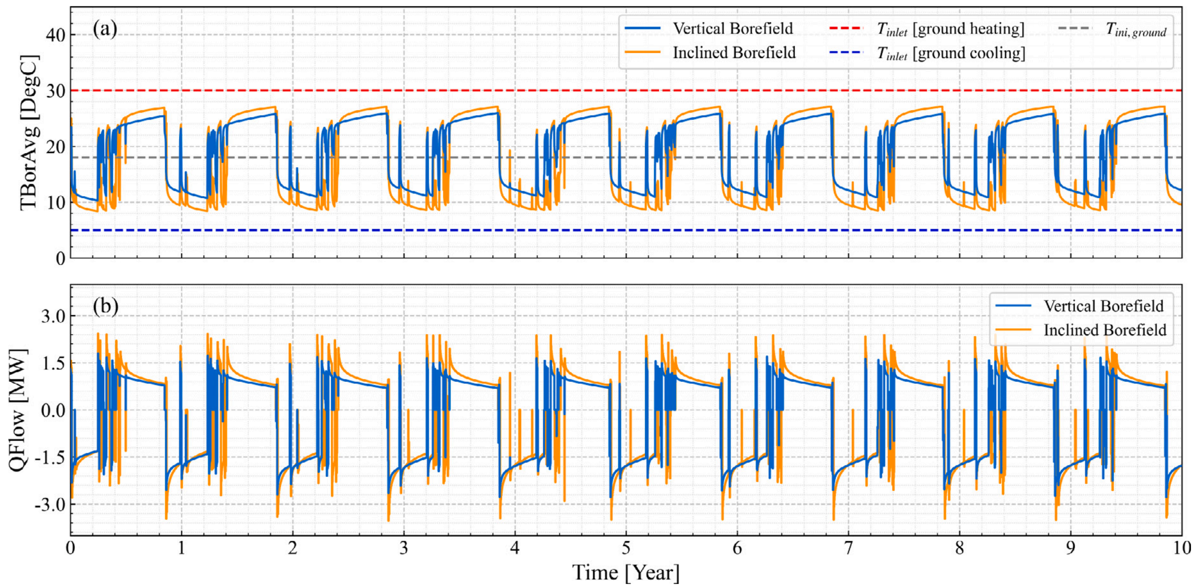

Fig. 15. Performance of BTES systems under the 10-year RH-MTS scenario: (a) Average borehole wall temperature (TBorAvg), where the red and blue dashed lines represent the maximum and minimum inlet temperatures, respectively, and the gray dashed line represents the initial ground temperature; (b) Total energy flow supplied by the BTES systems, where negative values indicate heat extraction from the ground (heating supply) and positive values indicate heat injection into the ground (cooling supply).

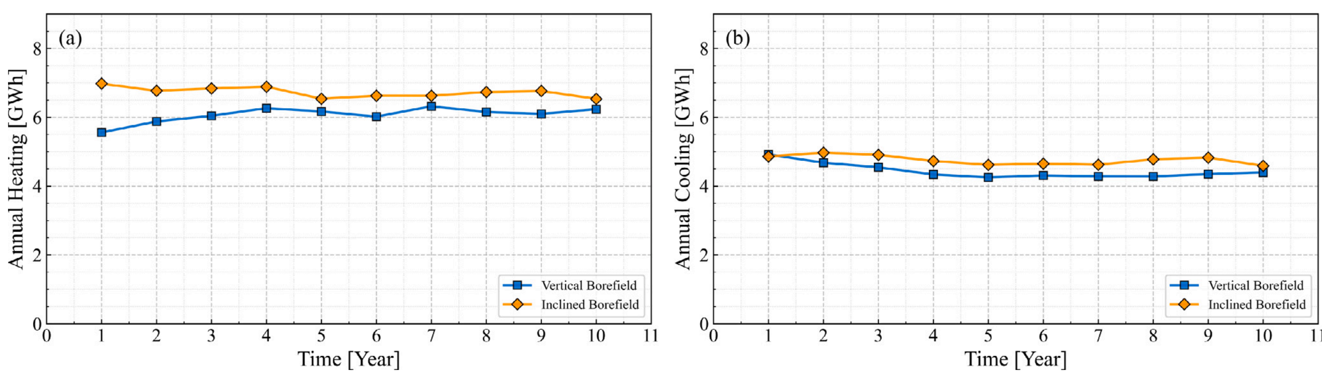

Fig. 16. Variation of annual heating and cooling energy supplies over 10 years using the RH-MTS method: (a) annual heating supply; (b) annual cooling supply.

In reality, flow rate and inlet temperature vary dynamically, as captured in Modelica, but such behavior cannot be represented in a linear MILP framework. The MILP g-function method is therefore best suited for large-scale DES optimization where some physical detail can be sacrificed. It provides more reliable estimates of shallow geothermal potential than constant heat transfer rate methods, while full-physics validation with Modelica remains essential to ensure feasibility and robustness, in line with PBD principles [38].

In the present work, BTES configurations are predefined based on site constraints and standard design guidelines. Extending the optimization framework to include borefield sizing and layout (e.g., number of boreholes and spacing) is an important direction for future work. However, directly embedding these variables into the MILP is challenging, as g-functions must be precomputed for each borefield configuration, introducing nonlinear relationships. A possible extension is to generate a set of candidate borefield designs with varying geometries (depth, spacing, pipe configuration) and include them as discrete options in the MILP, with integer variables selecting among alternatives. This would enable coupled techno-economic optimization of BTES design and operation, at the cost of increased computational complexity.

7.3. Validation of the MILP g-function method

The MILP g-function and RH-MTS methods developed in this study enable the integration of BTES into DES optimization. Results presented above demonstrate both reliability and scalability, but further validation with full-physics Modelica simulations remains a priority. Current validation was conducted against an example from the Modelica Buildings Library: a reservoir network with a BTES of 350 boreholes (300 m each). In this configuration, the BTES is clearly oversized relative to demand, so no noticeable decline in BTES output or changing rate of ground temperature is observed (Fig. 7). The strong agreement between MILP and Modelica results can partially be attributed to the simplicity of this case. By contrast, in the Berkeley campus case study, energy demand exceeds BTES capacity by more than an order of magnitude, resulting in a decline in borefield output (35%–65%, depending on conditions). Comparing this decline behavior between MILP and Modelica would provide more meaningful validation. However, no comparable DES example with high demand and undersized BTES is currently available in the Modelica Buildings Library. Developing such a case would require constructing a new system model, control strategy, and calibration, which lies beyond the scope of this study but represents an important direction for future work.

7.4. Limitations of the RH-MTS method

The RH-MTS method has proven effective in reducing solution time with only minor losses in optimality, a benefit that becomes critical as model complexity increases (e.g., with multiple BTES systems, additional hubs, or longer horizons). In preliminary tests, a model with two BTES systems and five hubs became intractable, motivating the development of RH-MTS. Its main limitation is the inevitable loss of accuracy from aggregating hourly variables into daily or monthly sub-horizons, which can smooth peak demands and underestimate capacities; this could be mitigated by incorporating a feedback loop that updates capacities as new lower bounds, which represents the next step of this study. A second limitation is the trade-off between accuracy and computation time, determined by sub-horizon lengths: longer horizons improve accuracy but increase solution time, while shorter horizons risk oversmoothing. To preserve seasonal patterns, the combined hourly and daily horizons should exceed six months; in this study, values of 2160, 150, and 3 for the hourly, daily, and monthly horizons, respectively, provided a good balance, though future applications may require adjustment.

8. Conclusions

This study develops a MILP g-function framework to enable accurate integration of the BTES system into large-scale DES optimization. To address the increased computational complexity associated with g-function coupling, a rolling horizon multi-time-step (RH-MTS) method is further proposed to improve model tractability while maintaining solution quality.

The principal findings of this study can be summarized as follows. First, the MILP g-function method is successfully validated against a full-physics Modelica reservoir network, indicating strong agreement in ground temperature and energy flow predictions, with annual energy supply deviations within 3%–6%, confirming its reliability. Second, the RH-MTS method effectively improves computational performance, reducing solution time by up to 73% while incurring only limited loss in optimality and preserving the operational patterns of BTES and other technologies.

The case study of the UC Berkeley campus demonstrates key insights into BTES performance. Although BTES contributes a modest share of total demand, it provides meaningful benefits in cost reduction and carbon mitigation, with an average energy cost of 0.70–0.77 USD/kWh and carbon intensity of 0.54 kg-CO_2/kWh. The results further reveal that BTES systems require approximately 4–5 years to reach stable operation, and that inclined borefields with double U-pipes achieve higher peak performance but exhibit greater seasonal decline, leading to comparable residual performance with vertical borefields. At present, the borefield layouts in this study are predefined based on site constraints thus may not represent the optimal design. Future work will extend the framework to include borefield sizing and layout optimization within the MILP.

Overall, this work advances the methodological development of shallow geothermal integration by providing a robust and computationally efficient framework for large-scale energy system optimization. The proposed approach enables systematic evaluation of BTES in district- and city-scale applications and offers practical support for decision-making in energy system decarbonization.

CRediT authorship contribution statement

Jiahui Yang: Writing – original draft, Visualization, Validation, Methodology, Formal analysis. **Kenichi Soga:** Writing – review & editing, Funding acquisition, Conceptualization. **Matthias Sulzer:** Writing – review & editing, Methodology, Conceptualization. **Kecheng Chen:** Writing – original draft, Methodology, Conceptualization.

Declaration of competing interest

The authors declare that they have no known competing financial interests or personal relationships that could have appeared to influence the work reported in this paper.

Acknowledgments

This study was based upon work supported by the U.S. Department of Energy (DOE), Office of Energy Efficiency and Renewable Energy (EERE), Geothermal Technologies Office, Low-Temperature Geothermal Program, under Award Number DE-AC02-05CH11231 with LBNL. The views expressed herein do not necessarily represent the views of the DOE or the U.S. Government.

Appendix. MILP formulation for DES optimization

The detailed formulation of the MILP-based DES model developed in this study is presented in this appendix. The general structure is similar to formulation presented in the literature, while minor difference exists.

A.1. Objective function components

The energy consumption cost in Eq. (A.1) consists of three components: the regular energy charge, the demand charge, and credits from exporting excess energy. For commercial and institutional buildings, demand charges can represent a substantial share of total energy costs and strongly influence operational strategies, particularly peak shaving strategy using storage systems.

$$\begin{aligned} C^{\text{Energy}} = & \sum_{ec}\sum_{t} \mathrm{P}^{\text{pur}}_{ec,t} \sum_{hub} Q^{\text{imp}}_{ec,hub,t} \\ & + \sum_{ec}\sum_{m} \mathrm{P}^{\text{dchar}}_{ec,m} \cdot \max_{h\in \text{Hour}_m} \left(\sum_{hub} Q^{\text{imp}}_{ec,hub,h} \right) \\ & - \sum_{ec}\sum_{t} \mathrm{P}^{\text{sal}}_{ec,t} \sum_{hub} Q^{\text{exp}}_{ec,hub,t} \end{aligned} \tag{A.1}$$

$$ec \in \text{Ec},\ t \in \text{T},\ hub \in \text{Hub},\ m \in \text{T}^{\text{month}}$$

The annualized investment cost is formulated in Eq. (A.2)–(A.3). Capital cost is expressed as a linear function of technology capacity, consisting of fixed and variable components. To distribute total investment uniformly over the technology lifetime, an annuity factor is applied, calculated from the specified lifetime and interest rate. A binary variable Bin_{tec} indicates the installation of technology tec, while Cap_{tec} denotes its capacity. To preserve MILP linearity, Bin_{tec} is applied only to the fixed term. The Constraint (A.7) ensures $Cap_{tec} = 0$ whenever $Bin_{tec} = 0$.

$$C^{\text{capex}} = \sum_{hub}\sum_{tec} A_{tec} (\mathrm{P}^{\text{fix}}_{tec} Bin_{hub,tec} + \mathrm{P}^{\text{var}}_{tec} Cap_{hub,tec}) \qquad hub \in \text{Hub},\ tec \in \text{Tec} \tag{A.2}$$

$$A_{tec} = \frac{\text{Irate}}{1 - \frac{1}{(1+\text{Irate})^{\text{life}_{tec}}}} \tag{A.3}$$

The O&M expense in Eq. (A.4) follows a similar structure to the annualized capital cost formulation, but without applying the annuity coefficient.

$$C^{\text{OM}} = \sum_{hub}\sum_{tec} \left(\mathrm{P}^{\text{fixOM}}_{tec} Bin_{hub,tec} + \mathrm{P}^{\text{varOM}}_{tec} Cap_{hub,tec} \right) \qquad hub \in \text{Hub},\ tec \in \text{Tec} \tag{A.4}$$

The carbon emissions of the system originate primarily from imported energy (natural gas and electricity in this study):

$$CO_2^{\text{Total}} = \sum_{ec}\sum_{t} \text{Car}_{ec,t} \sum_{hub} Q^{\text{imp}}_{ec,hub,t} \qquad ec \in \text{Ec},\ t \in \text{T},\ hub \in \text{Hub} \tag{A.5}$$

A.2. Energy carrier balance

Energy carriers are defined to represent the flow of energy through the system, encompassing imports, intermediate conversions, and demand satisfaction. The energy balance constraint in Eq. (A.6) must hold for each energy carrier ec, in each hub hub, and at each time step t. For instance, electricity may be supplied from imports or on-site generation (e.g., solar PV, cogeneration plants) and can be allocated to exports (e.g., sales to the grid), technology consumption, or end-use demand.

$$Q^{\text{imp}}_{ec,hub,t} + \sum_{tec \in \text{Tec}^{\text{gen}}_{ec}} Q^{\text{gen}}_{ec,hub,tec,t} = Q^{\text{exp}}_{ec,hub,t} + \sum_{tec \in \text{Tec}^{\text{con}}_{ec}} Q^{\text{con}}_{ec,hub,tec,t} + Q^{\text{dem}}_{ec,hub,t} \quad \forall\, ec \in \text{Ec},\ hub \in \text{Hub},\ t \in \text{T} \tag{A.6}$$

A.3. Energy technologies

Energy conversion technologies are formulated in Eq. (A.7). This representation applies to most technologies that convert one form of energy into another and provides a flexible way to model energy conversion processes within the MILP framework.

$$\begin{aligned} Q^{\text{con}}_{ec^{\text{in}},hub,tec,t} \cdot \text{COP}_{tec,ec^{\text{in}},ec^{\text{out}}} &= Q^{\text{gen}}_{ec^{\text{out}},hub,tec,t} \\ Q^{\text{gen}}_{ec^{\text{out}},hub,tec,t} &\le Cap_{hub,tec} \le \text{Cap}^{\max}_{hub,tec} \\ Cap_{hub,tec} &\le \text{M} \cdot Bin_{hub,tec} \end{aligned} \tag{A.7}$$

$\forall\,(tec, ec^{\text{in}}, ec^{\text{out}}) \in \text{Tup}^{\text{conv}},\ hub \in \text{Hub},\ t \in \text{T}$

Solar photovoltaic (PV) generation is modeled using a measured solar profile. While PV output generally depends on location and panel efficiency, modern commercial panels exhibit similar efficiencies. As this study focuses on the Bay Area, California, a PV generation profile measured on the UC Berkeley campus is employed to estimate electricity production, as formulated in Eq. (A.8).

$$\begin{aligned} Q^{\text{gen}}_{ec,hub,tec,t} &= \text{Solar}_t \cdot Area_{hub,tec} \\ Area_{hub,tec} &\le \text{Area}^{\max}_{hub,tec} \\ Area_{hub,tec} &\le \text{M} \cdot Bin_{hub,tec} \end{aligned} \tag{A.8}$$

$\forall\,(tec, ec) \in \text{Tup}^{\text{solar}},\ hub \in \text{Hub},\ t \in \text{T}$

Battery storage is modeled using the cyclic storage constraint in Eq. (A.9), which incorporates storage efficiency and round-trip charging/discharging efficiencies. The associated capacity constraint in Eq. (A.10) limits both the maximum state of storage and the allowable charging/discharging rates.

$$\begin{aligned} S_{hub,tec,t_0} &= \eta^{\text{sto}}_{tec} \cdot S_{hub,tec,t_{\text{end}}} - \frac{Q^{\text{gen}}_{ec,hub,tec,t_{\text{end}}}}{\eta^{\text{dis}}_{tec}} + Q^{\text{con}}_{ec,hub,tec,t_{\text{end}}} \cdot \eta^{\text{char}}_{tec} \\ S_{ec,hub,tec,t+1} &= \eta^{\text{sto}}_{tec} \cdot S_{ec,hub,tec,t} - \frac{Q^{\text{gen}}_{ec,hub,tec,t}}{\eta^{\text{dis}}_{tec}} + Q^{\text{con}}_{ec,hub,tec,t} \cdot \eta^{\text{char}}_{tec} \\ &\forall\,(tec, ec) \in \text{Tup}^{\text{battery}},\ hub \in \text{Hub},\ t \in \text{T} \setminus \{\text{t}_{\text{end}}\} \end{aligned} \tag{A.9}$$

$$\begin{aligned} S_{ec,hub,tec,t} &\le Cap_{hub,tec} \le \text{Cap}^{\max}_{hub,tec} \\ Q^{\text{gen}}_{ec,hub,tec,t} &\le Cap_{hub,tec} \cdot \eta^{\text{rate}}_{tec} \\ Cap_{hub,tec} &\le \text{M} \cdot Bin_{hub,tec} \end{aligned} \tag{A.10}$$

$\forall\,(tec, ec) \in \text{Tup}^{\text{battery}},\ hub \in \text{Hub},\ t \in \text{T}$

Stratified water tank is modeled in Eqs. (A.11)–(A.13). Different from conventional hot/cold water tanks, a stratified tank enforces a volume balance by matching inflow and outflow in Eq. (A.12), thereby improving operational efficiency. The stored energy $S_{ec,hub,tec,t}$ is represented as a continuous real variable, where a positive value indicates heating energy is stored, and a negative value means cooling energy is stored.

$$\begin{aligned} S_{hub,tec,t_0} &= \eta^{\text{sto}}_{tec} \cdot S_{hub,tec,t_{\text{end}}} - \frac{Q^{\text{gen}}_{ec^{\text{hea}},hub,tec,t_{\text{end}}}}{\eta^{\text{dis}}_{tec}} + \eta^{\text{char}}_{tec} \cdot Q^{\text{con}}_{ec^{\text{hea}},hub,tec,t_{\text{end}}} + \frac{Q^{\text{gen}}_{ec^{\text{coo}},hub,tec,t_{\text{end}}}}{\eta^{\text{dis}}_{tec}} - \eta^{\text{char}}_{tec} \cdot Q^{\text{con}}_{ec^{\text{coo}},hub,tec,t_{\text{end}}} \\ S_{hub,tec,t} &= \eta^{\text{sto}}_{tec} \cdot S_{hub,tec,t} - \frac{Q^{\text{gen}}_{ec^{\text{hea}},hub,tec,t}}{\eta^{\text{dis}}_{tec}} + \eta^{\text{char}}_{tec} \cdot Q^{\text{con}}_{ec^{\text{hea}},hub,tec,t} + \frac{Q^{\text{gen}}_{ec^{\text{coo}},hub,tec,t}}{\eta^{\text{dis}}_{tec}} - \eta^{\text{char}}_{tec} \cdot Q^{\text{con}}_{ec^{\text{coo}},hub,tec,t} \end{aligned} \tag{A.11}$$

$\forall\,(tec, ec^{\text{hea}}, ec^{\text{coo}}) \in \text{Tup}^{\text{tank}},\ hub \in \text{Hub},\ t \in \text{T} \setminus \{\text{t}_{\text{end}}\}$

$$\begin{aligned} Q^{\text{gen}}_{ec^{\text{hea}},hub,tec,t} &= Q^{\text{con}}_{ec^{\text{coo}},hub,tec,t} \\ Q^{\text{gen}}_{ec^{\text{coo}},hub,tec,t} &= Q^{\text{con}}_{ec^{\text{hea}},hub,tec,t} \end{aligned} \tag{A.12}$$

$\forall\,(tec, ec^{\text{hea}}, ec^{\text{coo}}) \in \text{Tup}^{\text{tank}},\ hub \in \text{Hub},\ t \in \text{T}$

$$\begin{aligned} S_{ec,hub,tec,t} &\le \text{Cap}_{hub,tec} \le Cap^{\max}_{hub,tec} \\ Q^{\text{gen}}_{ec^{\text{hea}},hub,tec,t} &\le Cap_{hub,tec} \cdot \eta^{\text{rate}}_{tec} \\ Q^{\text{gen}}_{ec^{\text{coo}},hub,tec,t} &\le Cap_{hub,tec} \cdot \eta^{\text{rate}}_{tec} \\ Cap_{hub,tec} &\le \text{M} \cdot Bin_{hub,tec} \end{aligned} \tag{A.13}$$

$\forall\,(tec, ec^{\text{hea}}, ec^{\text{coo}}) \in \text{Tup}^{\text{tank}},\ hub \in \text{Hub},\ t \in \text{T}$

Data availability

Data will be made available on request.

References

[1] Slameršak A, Kallis G, O'Neill DW. Energy requirements and carbon emissions for a low-carbon energy transition. Nat Commun 2022;13(1):6932.

[2] Sgouridis S, Csala D, Bardi U. The sower's way: quantifying the narrowing net-energy pathways to a global energy transition. Environ Res Lett 2016;11(9):094009.

[3] US Department of Energy. Quadrennial technology review: An assessment of energy technologies and research opportunities. Tech. rep., Washington, DC: U.S. Department of Energy; 2011, URL https://energy.gov/qtr.

[4] Billerbeck A, Breitschopf B, Preuß S, Winkler J, Ragwitz M, Keles D. Perception of district heating in europe: A deep dive into influencing factors and the role of regulation. Energy Policy 2024;184:113860.

[5] Figueira JS, Gil AG, Vieira A, Michopoulos AK, Boon DP, Loveridge F, Cecinato F, Götzl G, Epting J, Zosseder K, et al. Shallow geothermal energy systems for district heating and cooling networks: Review and technological progression through case studies. Renew Energy 2024;236:121436.

[6] Yang T, Liu W, Kramer GJ, Sun Q, et al. Seasonal thermal energy storage: A techno-economic literature review. Renew Sustain Energy Rev 2021;139:1–22.

[7] Sadeghi H, Jalali R, Singh RM. A review of borehole thermal energy storage and its integration into district heating systems. Renew Sustain Energy Rev 2024;192:114236.

[8] Wang X, Zhang H, Cui L, Wang J, Lee C, Zhu X, Dong Y. Borehole thermal energy storage for building heating application: A review. Renew Sustain Energy Rev 2024;203:114772.

[9] Witte H, Van Gelder A. Three years monitoring of a borehole thermal energy store of a UK office building. In: Thermal energy storage for sustainable energy consumption: fundamentals, case studies and design. Springer; 2007, p. 205–19.

[10] Sibbitt B, McClenahan D, Djebbar R, Thornton J, Wong B, Carriere J, Kokko J. The performance of a high solar fraction seasonal storage district heating system–five years of operation. Energy Procedia 2012;30:856–65.

[11] Flynn C, Sirén K. Influence of location and design on the performance of a solar district heating system equipped with borehole seasonal storage. Renew Energy 2015;81:377–88.

[12] Nilsson E, Rohdin P. Performance evaluation of an industrial borehole thermal energy storage (BTES) project–experiences from the first seven years of operation. Renew Energy 2019;143:1022–34.

[13] Bozkaya B, Li R, Zeiler W. A dynamic building and aquifer co-simulation method for thermal imbalance investigation. Appl Therm Eng 2018;144:681–94.

[14] Welsch B, Rühaak W, Schulte DO, Formhals J, Bär K, Sass I. Co-simulation of geothermal applications and HVAC systems. Energy Proc 2017;125:345–52.

[15] Liu Y, Mei X, Zhang G, Cao Z. Long-term performance prediction of ground source heat pump system based on co-simulation and artificial neural network. J Build Eng 2023;79:107949.

[16] Hu J, Doughty C, Dobson P, Nico P, Wetter M. Coupling subsurface and above-surface models for design of borefields and geothermal district heating and cooling systems. In: Proceedings, 45th workshop on geothermal reservoir engineering. 2020.

[17] Doughtry C, Hu J, Dobson P, Nico P, Wetter M. Coupling subsurface and above-surface models for optimizing the design of borefields and district heating and cooling systems in the presence of varying water-table depth. In: Proceedings, 46th workshop on geothermal reservoir engineering. Tech. rep., Lawrence Berkeley National Lab.(LBNL), Berkeley, CA (United States); 2022.

[18] Liu J, Wang F, Cai W, Wang Z, Li C. Numerical investigation on the effects of geological parameters and layered subsurface on the thermal performance of medium-deep borehole heat exchanger. Renew Energy 2020;149:384–99.

[19] Pandey U, Basu D. Effect of groundwater flow on thermal performance of SBTES systems. J Energy Storage 2023;74:109375.

[20] Li M, Lai AC. Review of analytical models for heat transfer by vertical ground heat exchangers (GHEs): A perspective of time and space scales. Appl Energy 2015;151:178–91.

[21] Eskilson P. Thermal analysis of heat extraction boreholes (Ph.D. thesis), Lund University of Technology; 1987.

[22] Claesson J, Eskilson P. Conductive heat extraction to a deep borehole: Thermal analyses and dimensioning rules. Energy 1988;13(6):509–27.

[23] Claesson J, Dunand A. Heat extraction from the ground by horizontal pipes: a mathematical analysis. Byggforskningsrådet (BFR); 1983.

[24] Hellstrom G. Ground heat storage: Thermal analyses of duct storage systems. I. Theory. 1992.

[25] Claesson J, Hellström G. Multipole method to calculate borehole thermal resistances in a borehole heat exchanger. Hvac&R Res 2011;17(6):895–911.

[26] Cimmino M, Bernier M. A semi-analytical method to generate g-functions for geothermal bore fields. Int J Heat Mass Transfer 2014;70:641–50.

[27] Cimmino M, Thorne D, Langevin C, Sukop M. Pygfunction: an open-source toolbox for the evaluation of thermal response factors for geothermal borehole fields. Proc ESim 2018;2018.

[28] Cimmino M. Semi-analytical method for g-function calculation of bore fields with series-and parallel-connected boreholes. Sci Technol the Built Environ 2019;25(8):1007–22.

[29] Peere W, Blanke T. GHEtool: An open-source tool for borefield sizing in Python. J Open Source Softw 2022;7(76):4406. http://dx.doi.org/10.21105/joss.04406.

[30] Cimmino M, Cook JC, Isiordia Farrera JA. Optimal discretization of geothermal boreholes for the calculation of g-functions. Sci Technol the Built Environ 2024;30(3):234–49.

[31] Miceli AV, Buscemi A, Guarino S, Beccali M, Brano VL. Modelling of borehole thermal energy storages: A g-function approach with a novel load aggregation scheme. Energy Convers Manage 2026;348:120666.

[32] Yang Y, Yang X, Lin C, Xu L, Wang Q, Xu S, Wu W. Novel discretization method to calculate g-functions of vertical geothermal boreholes with improved accuracy and efficiency. Renew Energy 2026;125547.

[33] Wetter M, Sulzer M. A call to action for building energy system modelling in the age of decarbonization. J Build Perform Simul 2024;17(3):383–93.

[34] Lázár E, Petreuş D, Etz R, Pătărău T. Minimization of operational cost for an islanded microgrid using a real coded genetic algorithm and a mixed integer linear programming method. In: 2017 international conference on optimization of electrical and electronic equipment (OPTIM) & 2017 intl aegean conference on electrical machines and power electronics. ACEMP, IEEE; 2017, p. 693–8.

[35] Polat U, Gürtuna F. A review of applications of linear programming and mixed integer linear programming in energy management: From policy makers/producers to consumers. Eur J Eng Appl Sci 2018;1(2):84–9.

[36] Lambert J, Ceruti A, Spliethoff H. Benchmark of mixed-integer linear programming formulations for district heating network design. Energy 2024;308:132885.

[37] Khan M, Shan-e Abbas S, Gulraiz A. Optimizing energy systems using mixed-integer linear programming. In: 2025 international conference on emerging power technologies. ICEPT, IEEE; 2025, p. 1–6.

[38] Sulzer M, Wetter M, Mutschler R, Sangiovanni-Vincentelli A. Platform-based design for energy systems. Appl Energy 2023;352:121955.

[39] Bollinger LA, Marquant J, Sulzer M. Optimization-based planning of local energy systems-bridging the research-practice gap. In: IOP conference series: earth and environmental science. Vol. 323, (1):IOP Publishing; 2019, 012077.

[40] Marquant JF. Multiscale urban energy system optimization using spatio-temporal clustering (Ph.D. thesis), ETH Zurich; 2018.

[41] Murray P, Marquant J, Niffeler M, Mavromatidis G, Orehounig K. Optimal transformation strategies for buildings, neighbourhoods and districts to reach CO2 emission reduction targets. Energy Build 2020;207:109569.

[42] Lin Y, Tang X, Fan X. Optimization of multi-energy grid for smart stadiums based on improved mixed integer linear algorithm. Energy Rep 2022;8:13417–24.

[43] Kamerling S, Vuillerme V, Rodat S. Solar field output temperature optimization using a MILP algorithm and a 0D model in the case of a hybrid concentrated solar thermal power plant for SHIP applications. Energies 2021;14(13):3731.

[44] Omu A, Hsieh S, Orehounig K. Mixed integer linear programming for the design of solar thermal energy systems with short-term storage. Appl Energy 2016;180:313–26.

[45] Steen D, Stadler M, Cardoso G, Groissböck M, DeForest N, Marnay C. Modeling of thermal storage systems in MILP distributed energy resource models. Appl Energy 2015;137:782–92.

[46] Hsieh S, Omu A, Orehounig K. Comparison of solar thermal systems with storage: From building to neighbourhood scale. Energy Build 2017;152:359–72.

[47] Lamedica R, Santini E, Ruvio A, Palagi L, Rossetta I. A MILP methodology to optimize sizing of PV-wind renewable energy systems. Energy 2018;165:385–98.

[48] Xia P, Deng C, Chen Y, Yao W. MILP based robust short-term scheduling for wind–thermal–hydro power system with pumped hydro energy storage. IEEE Access 2019;7:30261–75.

[49] Wędzik A, Siewierski T, Szypowski M. A new method for simultaneous optimizing of wind farm's network layout and cable cross-sections by MILP optimization. Appl Energy 2016;182:525–38.

[50] Guedes LS, de Mendonça Maia P, Lisboa AC, Vieira DAG, Saldanha RR. A unit commitment algorithm and a compact MILP model for short-term hydro-power generation scheduling. IEEE Trans Power Syst 2016;32(5):3381–90.

[51] Humbert G, Beermann D, Mutschler R, Sulzer M. Optimizing borehole thermal energy storage (BTES) system integration: A platform-based design approach with mixed-integer linear programming. J Phys: Conf Series 2025;3140(2):022024.

[52] Fiorentini M, Heer P, Baldini L. Design optimization of a district heating and cooling system with a borehole seasonal thermal energy storage. Energy 2023;262:125464.

[53] Blanke T, Born H, Döring B, Göttsche J, Herrmann U, Frisch J, van Treeck C. Model for dimensioning borehole heat exchanger applied to mixed-integer-linear-problem (MILP) energy system optimization. Geotherm Energy 2024;12(1):30.

[54] Grossmann IE. Advances in mathematical programming models for enterprise-wide optimization. Comput Chem Eng 2012;47:2–18.

[55] Mavromatidis G, Orehounig K, Bollinger LA, Hohmann M, Marquant JF, Miglani S, Morvaj B, Murray P, Waibel C, Wang D, et al. Ten questions concerning modeling of distributed multi-energy systems. Build Environ 2019;165:106372.

[56] Domínguez-Muñoz F, Cejudo-López JM, Carrillo-Andrés A, Gallardo-Salazar M. Selection of typical demand days for CHP optimization. Energy Build 2011;43(11):3036–43.

[57] Marquant JF, Evins R, Carmeliet J. Reducing computation time with a rolling horizon approach applied to a MILP formulation of multiple urban energy hub system. Procedia Comput Sci 2015;51:2137–46.

[58] Erichsen G, Zimmermann T, Kather A. Effect of different interval lengths in a rolling horizon MILP unit commitment with non-linear control model for a small energy system. Energies 2019;12(6):1003.

[59] Wang H, Meng K, Dong ZY, Xu Z, Luo F, Wong KP. Efficient real-time residential energy management through MILP based rolling horizon optimization. In: 2015 IEEE power & energy society general meeting. IEEE; 2015, p. 1–6.

[60] Malysz P, Sirouspour S, Emadi A. MILP-based rolling horizon control for microgrids with battery storage. In: IECON 2013-39th annual conference of the IEEE industrial electronics society. IEEE; 2013, p. 2099–104.

[61] Papadimitriou D, Fortz B. A rolling horizon heuristic for the multiperiod network design and routing problem. Networks 2015;66(4):364–79.

[62] Zhang B, Wakui T, Aoji S. Optimal design of energy storage-supply systems using a multi-objective evolutionary algorithm and mixed-integer linear programming with a two-stage rolling horizon method. Energy 2025;137970.

[63] Cimmino M, Bernier M, Adams F. A contribution towards the determination of g-functions using the finite line source. Appl Therm Eng 2013;51(1–2):401–12.

[64] Spitler J, Bernier M. Vertical borehole ground heat exchanger design methods. In: Advances in ground-source heat pump systems. Elsevier; 2016, p. 29–61.

[65] Yang J, Chen K, Soga K. Geothermal investigation on the UC berkeley campus. In: Proceedings, 49th workshop on geothermal reservoir engineering. stanford, CA: stanford university; 2024.

[66] Celsius Energy. SLB renovates its technological center in Clamart, Paris Region. 2020, URL https://www.celsiusenergy.com/us/our-portfolio/slb-renovates-its-technological-center-in-clamart-paris-region/, (Accessed: 2025-08-05).

[67] SLB. Celsius energy helps framingham state university reduce carbon footprint. 2024, URL https://www.slb.com/resource-library/case-study-with-navigation/sne/celsius-framingham-us-cs, (Accessed: 2025-08-05).

[68] Geidl M, Andersson G. Optimal coupling of energy infrastructures. In: 2007 IEEE lausanne power tech. IEEE; 2007, p. 1398–403.

[69] Geidl M, Koeppel G, Favre-Perrod P, Klockl B, Andersson G, Frohlich K. Energy hubs for the future. IEEE Power Energy Mag 2007;5(1):24–30.

[70] Geidl M, Koeppel G, Favre-Perrod P, Klöckl B, Andersson G, Fröhlich K. The energy hub–a powerful concept for future energy systems. In: Third annual carnegie mellon conference on the electricity industry. Vol. 13, Carnegie Mellon University Pittsburgh; 2007, p. 14.

[71] Pareto V. Cours d'économie politique. vol. 1, Librairie Droz; 1964.

[72] Coello Coello CA. A comprehensive survey of evolutionary-based multiobjective optimization techniques. Knowl Inf Syst 1999;1(3):269–308.

[73] Miettinen K. Nonlinear multiobjective optimization. vol. 12, Springer Science & Business Media; 1999.

[74] Lazzaretto A, Toffolo A. Energy, economy and environment as objectives in multi-criterion optimization of thermal systems design. Energy 2004;29(8):1139–57.

[75] Liu C-H, Huang D-H. Reduction of power consumption and carbon footprints by applying multi-objective optimisation via genetic algorithms. Int J Prod Res 2014;52(2):337–52.

[76] Li S, Bei J, Wu Z, Wu B, Zhu Z. Low carbon design of automobile front-end structure based on Pareto mining. Int J Veh Des 2024;95(1–2):114–36.

[77] Research conference proceedings, IGSHPA annual conference 2022. In: Research conference proceedings, IGSHPA annual conference 2022. International Ground Source Heat Pump Association; 2022, http://dx.doi.org/10.22488/okstate.22.000010.

[78] Wetter M, Zuo W, Nouidui TS, Pang X. Modelica buildings library. J Build Perform Simul 2014;7(4):253–70.

[79] Sommer T, Sulzer M, Wetter M, Sotnikov A, Mennel S, Stettler C. The reservoir network: A new network topology for district heating and cooling. Energy 2020;199:117418.

[80] Laferrière A, Cimmino M, Picard D, Helsen L. Development and validation of a full-time-scale semi-analytical model for the short-and long-term simulation of vertical geothermal bore fields. Geothermics 2020;86:101788.

[81] University of California, Berkeley. Clean energy campus: Integrated resource & activation plan (IRAP). 2023, URL https://cleanenergycampus.berkeley.edu/, Prepared by Facilities Services and the Office of Sustainability & Carbon Solutions.

[82] UC Berkeley Facilities. Internal energy consumption data and reports for campus buildings. 2023, Unpublished internal document, University of California, Berkeley.

[83] Pacific Gas and Electric Company. Electric Schedule B-20, Sheet 4. 2025, URL https://www.pge.com/tariffs/assets/pdf/tariffbook/ELEC_SCHEDS_B-20.pdf.

[84] California Air Resources Board. 2023 carbon intensity values for california average grid electricity used as a transportation fuel in california and electricity supplied under the smart charging or smart electrolysis provision. Tech. rep, California Air Resources Board; 2022, URL https://ww2.arb.ca.gov/sites/default/files/classic/fuels/lcfs/fuelpathways/comments/tier2/2023_elec_update.pdf, Low Carbon Fuel Standard Program.